JGR Space Physics

RESEARCH ARTICLE
10.1029/2024JA033231

# Categorization of Electron Isotropy Boundary Patterns: ELFIN and POES Observations

A. V. Artemyev[1,2], V. A. Sergeev[3], V. Angelopoulos[1], X.-J. Zhang[4], and C. Wilkins[1]

[1]Department of Earth, Planetary, and Space Sciences, University of California, Los Angeles, CA, USA, [2]Space Research Institute, RAS, Moscow, Russia, [3]Department of Earth Physics, St. Petersburg State University, St. Petersburg, Russia, [4]Department of Physics, University of Texas at Dallas, Richardson, TX, USA

**Key Points:**

- We categorize of energy-dependent electron isotropy boundary (IB) patterns using high energy range and resolution of ELFIN observations
- We demonstrate approaches for distinguishing patterns produced by non-adiabatic magnetic curvature and wave-particle resonant scattering
- Plenty of non-monotonic, or steep, even multiple, IB patterns suggest abundance of non-trivial tail current sheet structure

**Correspondence to:**
A. V. Artemyev,
aartemyev@igpp.ucla.edu

**Citation:**
Artemyev, A. V., Sergeev, V. A., Angelopoulos, V., Zhang, X.-J., & Wilkins, C. (2024). Categorization of electron isotropy boundary patterns: ELFIN and POES observations. *Journal of Geophysical Research: Space Physics*, *129*, e2024JA033231. https://doi.org/10.1029/2024JA033231

Received 27 AUG 2024
Accepted 20 NOV 2024

**Abstract** Magnetic field-line curvature scattering (FLCS) of energetic particles in the equatorial magnetotail results in isotropization of pitch-angle distributions, loss-cone filling, and precipitation above a minimum energy at a given latitude. At a fixed energy, the lowest latitude of isotropization is the isotropy boundary (IB) for that energy. Nominally, the IB (latitude) exhibits a characteristic energy dependence due to the monotonic variation of the equatorial magnetic field intensity $B_{eq}$ with radial distance. Deviations from this nominal IB dispersion can occur if the radial $B_{eq}$ variation (spatial or temporal) is non-mononotic and/or if other precipitation mechanisms prevail. With its sensitive and detailed measurements of electron spectra up to relativistic energies, ELFIN's recent observations reveal a variety of electron IBe patterns near magnetic midnight which are repeatable enough to warrant classification. This study aims to categorize the various IBe patterns observed by ELFIN's high-fidelity but short lived dataset (a few months), compare them with simultaneous nearby POES observations, which are made with a limited energy coverage and resolution but last for decades, and discuss their possible interpretation. The general agreement between ELFIN and POES IB observations indicate a relatively large-scale nature of IBe patterns. Surprisingly, there exists a large number (up to 2/3 of all events) of non-monotonic-or steep/multiple-IB patterns. This suggest an abundance of non-trivial tail current sheet structures or a mixed contribution of two mechanisms in the vicinity of IBe in these cases.

**Plain Language Summary** Energetic particle scattering by magnetic field-line curvature (FLCS) in the equatorial magnetotail forms isotropic loss-cone precipitation. Its equatorward boundary (so-called isotropy boundary, IB) displays a remarkably distinguishable pattern where the latitude decreases with increasing particle energy (rigidity) if the equatorial magnetic field $B_{eq}$ decreases monotonically with a distance in the magnetotail. Deviations from simple dispersion patterns can occur in non-monotonic radial $B_{eq}$ variation regions and/or in the presence of other precipitation mechanisms. With its sensitive and detailed measurements of electron spectra up to relativistic energies, recent ELFIN CubeSat observations demonstrate a variety of patterns of electron IBe appearance. This study aims to categorize various IBe patterns, discuss their possible interpretations, and link them to the vast information about electron and ion IBs that have been accumulated by low-altitude POES spacecraft, although obtained with a limited energy coverage and resolution. Further investigation of these IBe patterns and conjugate in situ magnetospheric observations is important to identify true FLCS boundary (ies) and use them to investigate the variable dynamical magnetospheric configuration of the transition from plasma sheet to the radiation belt.

## 1. Introduction

There are two main mechanisms capable of providing intense isotropic energetic electron precipitation from the near-Earth's magnetosphere: wave-particle resonant interactions (WPI) and non-adiabatic electron scattering by magnetic field-line curvature (through the paper, magnetic field-line curvature scattering, or FLCS). The former (group of) mechanism primarily operates in the Earth's radiation belts and involves electron scattering by whistler-mode and ion cyclotron waves (Kasahara et al., 2018; R. Millan & Thorne, 2007; Shprits et al., 2008; Thorne et al., 2021), but also can be responsible for plasma sheet electron scattering by whistler-mode waves (see Ni et al., 2016; Nishimura et al., 2010), electron cyclotron harmonics (see Ni, Thorne, Horne, et al., 2011; Zhang et al., 2015), broadband electrostatic noise (see Shen et al., 2020, and references therein), and kinetic Alfven waves (see Shen et al., 2022, and references therein). The latter mechanism operates in the near-Earth plasma sheet where the curvature radius is sufficiently small in the tail current sheet to support the scattering of energetic electrons (Birmingham, 1984; Büchner & Zelenyi, 1989; Sergeev & Tsyganenko, 1982; West et al., 1978). The

inner (earthward) edge of this thin current sheet may intrude to low radial distances, and the curvature scattering can potentially provide isotropic bounce loss-cone precipitation and rapid losses of the energetic and relativistic electrons from the nightside portion of the outer radiation belt (Artemyev, Angelopoulos, et al., 2022; Sergeev et al., 2012; Zou et al., 2024). Correspondingly, at low altitudes, the isotropy boundary (IB) can be determined at any particular energy, which demarcates the isotropic loss cone precipitated fluxes (on the poleward side) from intense anisotropic fluxes in the radiation belt proper (on the equatorward side). The morphology of the proton IBs, which are formed in strong magnetic fields of several tens nT and are observed at any local time, was studied in dozens of publications (Dubyagin et al., 2018; Ganushkina et al., 2005; Gvozdevsky et al., 1997; Lvova et al., 2005; Newell et al., 1998; Sergeev et al., 1983, 1997, 2015; Shi et al., 2024; Yue et al., 2014) and is relatively well-explored by now. As regards energetic electrons, in the absence of strong (rare) solar electron fluxes, for electrons the IB is mostly detected in the nightside local time sector (e.g., Bikkuzina et al., 1998; Imhof et al., 1979; Wilkins et al., 2023) where IB intrudes into the radiation belt, so and its morphology is less thoroughly investigated.

General interest in the isotropy boundary studies is motivated by its unique nature and consequences in the case of the FLCS mechanism: if the IB observed at low altitude at particular energy corresponds to the FLCS boundary which is formed and controlled by an equatorial magnetic field, this provides an attractive possibility to control mapping and get information on the field-line stretching in the equatorial magnetosphere (see, e.g., Sergeev & Gvozdevsky, 1995; Wing & Newell, 1998; Sotirelis & Newell, 2000; Sergeev et al., 2012, 2023; Shi et al., 2024). Even more, in case the energy-dependent (and species-dependent) IB locations are known during the auroral zone traversed by polar spacecraft (it is referred to after that as the IB pattern), this, in principle, can be used to reconstruct the equatorial magnetic field radial profile based on low-altitude observations. On the other hand, in the presence of other (WPI-type) mechanisms capable of causing the isotropic precipitation, the distinction between WPI and FLCS contributions (i.e.,.- where is a true FLCS boundary?) may be a complicated problem, especially during disturbed conditions (see, e.g., Gvozdevsky et al., 1997). The information about the isotropy boundary pattern can help immensely in answering this question.

Unfortunately, the information about the IB pattern is rather limited because of insufficient sensitivity and energy resolution of past spacecraft instruments. For a long time, the Polar Operational Environmental Satellites (POES) provided basic information for studying the IB variations at fixed energies. Still, they possess sparse energy resolution of ion and electron detectors (Evans & Greer, 2004; Yando et al., 2011). Fortunately, this has been recently resolved with the help of new very sensitive energetic electron measurements at low-altitudes by ELFIN CubeSat mission that provides full pitch-angle distribution with good energy resolution (16 logarithmically distributed energy channels between 50 keV and 6 MeV; see Angelopoulos et al., 2020). ELFIN measurements resolve well electron IB for 3 years of spacecraft observations (Wilkins et al., 2023). In this paper, we use these ELFIN observations to systematize/categorize the peculiarities of electron IB patterns, attempt to separate WPI- and FLCS-induced effects, and discuss what can be interpreted of various peculiarities in terms of the FLCS mechanism. We also compare the simultaneous ELFIN/POES observations during a few nearby auroral zone traversals comparison for several of the most interesting electron IB examples to ensure their consistency and get some information about the azimuthal scale size of structures.

## 2. Data Sets

We focus on the ELFIN dataset collected in July-September 2022 when both electron and ion energetic particle detectors (EPDe and EPDi) were operating and providing measurements in the night-side magnetosphere. EPD covers the energy range from 50 keV to 6 MeV with 16 logarithmically distributed energy bins and a full pitch-angle range $[0, 180°]$ with 22.5° channel width (Angelopoulos et al., 2020; Tsai, Palla, et al., 2024). The time resolution of EPD collection of full energy, pitch-angle distribution is 3 s (ELFIN spin). ELFIN's altitude is ∼450km, and the orbital period is about 90 min. The typical interval of downloaded ELFIN measurements, science zone, covers the number of magnetic field lines projected to the equator from the plasmasphere ($L$-shell about 4) to the plasmasheet ($L$-shell about 10–20). One science zone takes about ∼5min intervals. Figure 1 shows the example of typical ELFIN orbit. The energy, pitch-angle distribution collected by ELFIN is reduced to the standard ELFIN data products: locally trapped fluxes $j_{trap}(E,t)$ (distribution integrated outside the bounce loss-cone; LC; see panels $a$, $c$ in Figure 1), precipitating fluxes $j_{prec}(E,t)$ (distribution integrated within the bounce loss-cone), and backscattered fluxes $j_{back}(E,t)$ (distribution integrated within the bounce anti-loss-cone). These

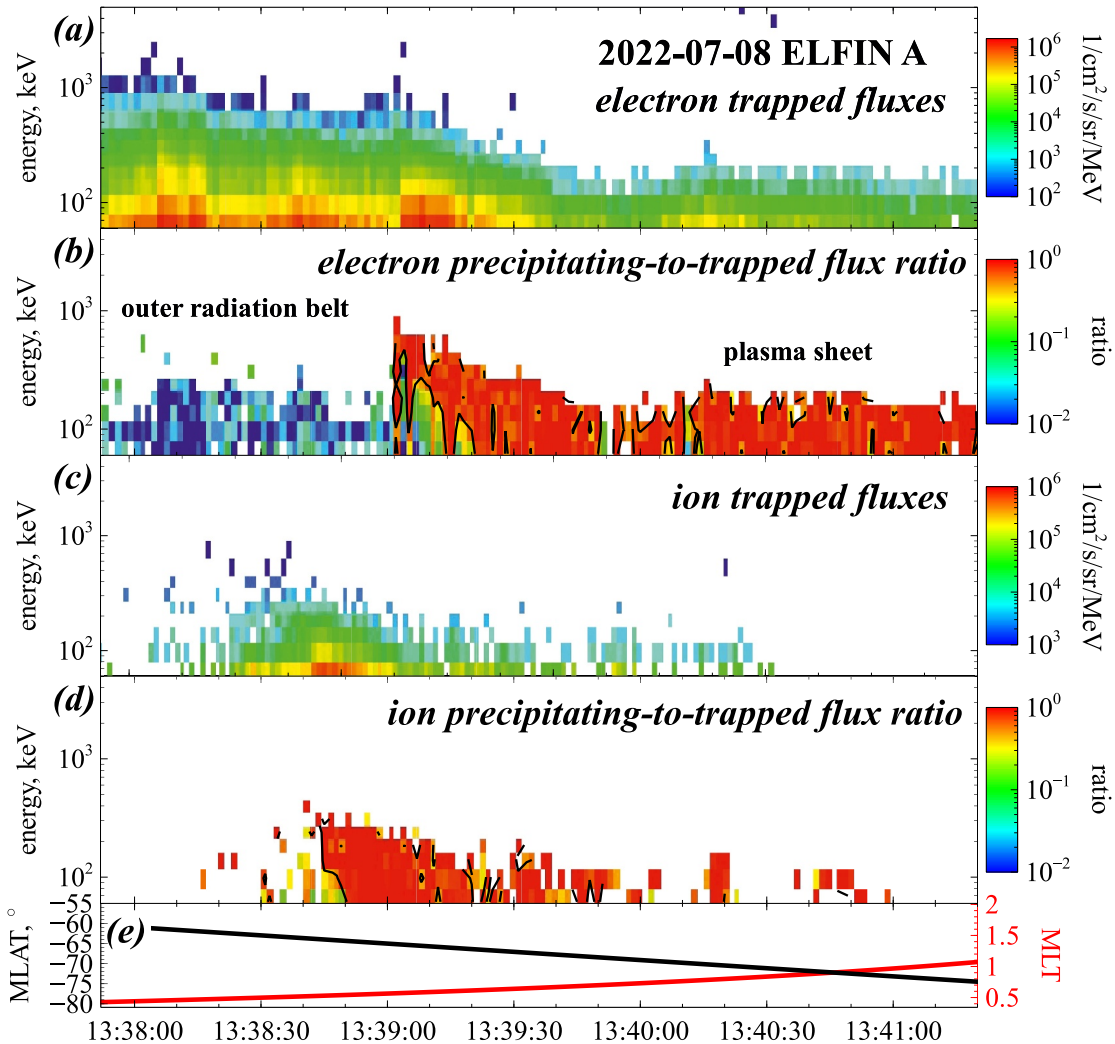


**Figure 1.** The ELFIN A orbit with main data products. From top to bottom: electron-trapped fluxes in $(cm^2\ s\ sr\ MeV)^{-1}$ (panel *a*), electron precipitating-to-trapped flux ratio (panel *b*), ion trapped fluxes in $(cm^2\ s\ sr\ MeV)^{-1}$ (panel *c*), ion precipitating-to-trapped flux ratio (panels *d*), ELFIN AACGM latitude in black and MLT in red (panel *e*).

data products evaluate the precipitating-to-trapped flux ratio, $R = j_{prec}/j_{trap}$ (see panels *b*, *d* in Figure 1). Note, at 450 km altitude most of the measured fluxes are within the drift loss-cone, and will be precipitated somewhere along the drift path (see discussion in Mourenas et al., 2021). Observations of $j_{prec}/j_{trap} \sim 0$ can be interpreted as an empty loss-cone when equatorial particle distribution is anisotropic and particles are not scattered in pitch-angle. Localized increases of $R$ can be interpreted as scattering of energetic particles. The strong diffusion regime with $R = j_{prec}/j_{trap} \approx 1$ (Kennel, 1969) can be interpreted as an equatorial flux isotropization and loss-cone filling due to strong pitch-angle scattering. This region is associated with either intense equatorial wave activity (e.g., Angelopoulos et al., 2023; Qin et al., 2024; Zhang et al., 2022) or curvature scattering in the equatorial plasma sheet (e.g., Wilkins et al., 2023). In this study, we will focus on the pattern of the transition region between isotropic plasma sheet fluxes, $R \approx 1$, and anisotropic fluxes of the inner magnetosphere, $R \sim 0$.

The altitude-adjusted corrected geomagnetic (AACGM) coordinates (e.g., Baker & Wing, 1989) are invaluable to order and compare the observed locations and to interpret them in the magnetospheric context (see panel *e* in Figure 1). We started from the geographic coordinates of spacecraft trajectory points for both ELFIN and POES. We mapped them along the magnetic field line using a sum of IGRF (inner) and T89 $Kp = 3$ (external) magnetic field modules until either the equatorial plane or $15R_E$ distance using Tsyganenko GEOPACK-08 programs. After that, we mapped back the magnetic field line using a sum of Dipole and T89 (Tsyganenko, 1989) modules until its

intersection with the Earth surface ($1R_E$) and used the solar-magnetic (SM) coordinates to get the AACGM latitude and magnetic local time (MLT) characterizing the spacecraft location.

The energetic particle observations (Evans & Greer, 2004) made by a suite of POES spacecraft flying on polar sun-synchronous orbits have been presented in numerous studies, so they need only a brief introduction. Here, we used data from MEPED instruments, including mostly three electron channels: E1, E2, E3, and E4 (having roughly 40, 130, 289, and 610 keV nominal thresholds, the last channel is pretty noisy), as well as 30 and 80 keV proton channels. The measurements of trapped ($J_{90}$) and precipitated ($J_0$) fluxes are provided by separate detectors, whose sensitivity may degrade differently during the lifetime of individual spacecraft. The 2 s time resolution of POES is comparable to ~3sec resolution of ELFIN, but sensitivity is an order as higher at ELFIN. The main advantage of POES observations is their excellent coverage in space and time due to up to six spacecraft being simultaneously in orbit and recording virtually every auroral zone crossing, which makes them invaluable in various studies of global magnetotail dynamics. On the contrary, high sensitivity, large energy range, and energy resolution make ELFIN a unique tool for IBe pattern recognition studies, which are of high value in distinguishing between WPI and FLCS mechanisms.

## 3. Categorization of Isotropic Precipitation Patterns

Energy dependence of the loss-cone filling pattern (IB pattern) provides an important distinctive property for identifying the origin/mechanism of isotropic precipitation. A fundamental distinction of the FLCS from WPI mechanisms is related to the fact that if the threshold condition for strong diffusion into the loss cone $(j_{prec}/j_{trap} \approx 1)$ is fulfilled for some critical energy $E_c$ in a particular plasma tube, then the isotropic precipitation is guaranteed there for any energy $E > E_c$. In contrast, the loss cone will be empty for any energy $E < E_c$. In the current sheet geometry, this critical energy is determined by the magnetic field line curvature radius (see details in Sergeev & Tsyganenko, 1982; Birmingham, 1984; Sergeev et al., 1983; Delcourt & Sauvaud, 1994) which critically depends on equatorial $B_{eq} \approx B_z$ component. The energy dependence of wave-particle resonance scattering (e.g., by whistler-mode waves, which are the strongest driver of isotropic precipitation in the midnight sector, see Tsai et al., 2022; Tsai, Artemyev, et al., 2024) is quite different, the largest scattering is expected near the resonant energies (tens keV; see, e.g., Summers, 2005; Ni, Thorne, Meredith, Shprits, & Horne, 2011; Ni, Thorne, Meredith, Horne, & Shprits, 2011), with weak precipitation normally expected at hundreds of keV-MeV energies. The great advantage of ELFIN EPD is its good sensitivity to the electron fluxes at high energies up to a few MeV (allowing to see the flux isotropy in the high-energy range) as well as excellent energy resolution, allowing to observe and study the energy-dispersed IB pattern in many details. This provides additional information to confirm the FLCS origin of isotropic precipitation and, when confirmed, make conclusions on the details of equatorial magnetic field distribution. In the average magnetospheric model, due to the monotonic decrease of the equatorial magnetic field magnitude with a distance from the Earth, the energy at the IB should progressively decrease with the latitude as it was previously reported (e.g., Imhof et al., 1979; Sergeev et al., 2012; Shi et al., 2024; Wilkins et al., 2023). Availability of proton isotropy boundary (IBp) observations during spacecraft traversal enhances the reliability of interpretation by confirming the spatial ordering of (more equatorward) IBp and (more poleward) IBe and provides the distance between them (which has to be roughly a couple degrees of magnetic latitude according to magnetospheric models,e.g. Shevchenko et al., 2010).

Due to high sensitivity and excellent energy resolution, ELFIN observations provide bright visual portraits of different IB dispersion patterns. In all events taken for illustration in Figures 2–4 below, ELFIN traversed poleward from the radiation belt (manifested by enhanced fluxes of relativistic electrons in the upper panels) to the plasma sheet where only low fluxes of lowest energy protons or electrons can sporadically be observed (to keep consistency, two orbits following in the direction from plasma sheet to the radiation belt are plotted here in the inverse time). Isotropic precipitation is nicely seen as red areas on $j_{prec}/j_{trap}$ ratio panels (second from top for electrons and fourth from top for protons).

Figures 2a–2f presents six examples of what can be considered the most simple and basic form of the IBe patterns in the nightside magnetosphere, in which the electron isotropy (red) region looks as the edge strip at the outer radiation belt (ORB) boundary. Such appearance is quite expectable from the fact that for sub- and relativistic electrons, the isotropic loss cone filling depletes very fast the near-Earth flux tubes (the electron lifetime is of the order of minutes-tens minutes for these particles at $L$-shell 7 to 10; see Kennel, 1969). Therefore, in the case of a nearly stable magnetic configuration, the ORB boundary will essentially be shaped by the IBe-related isotropic

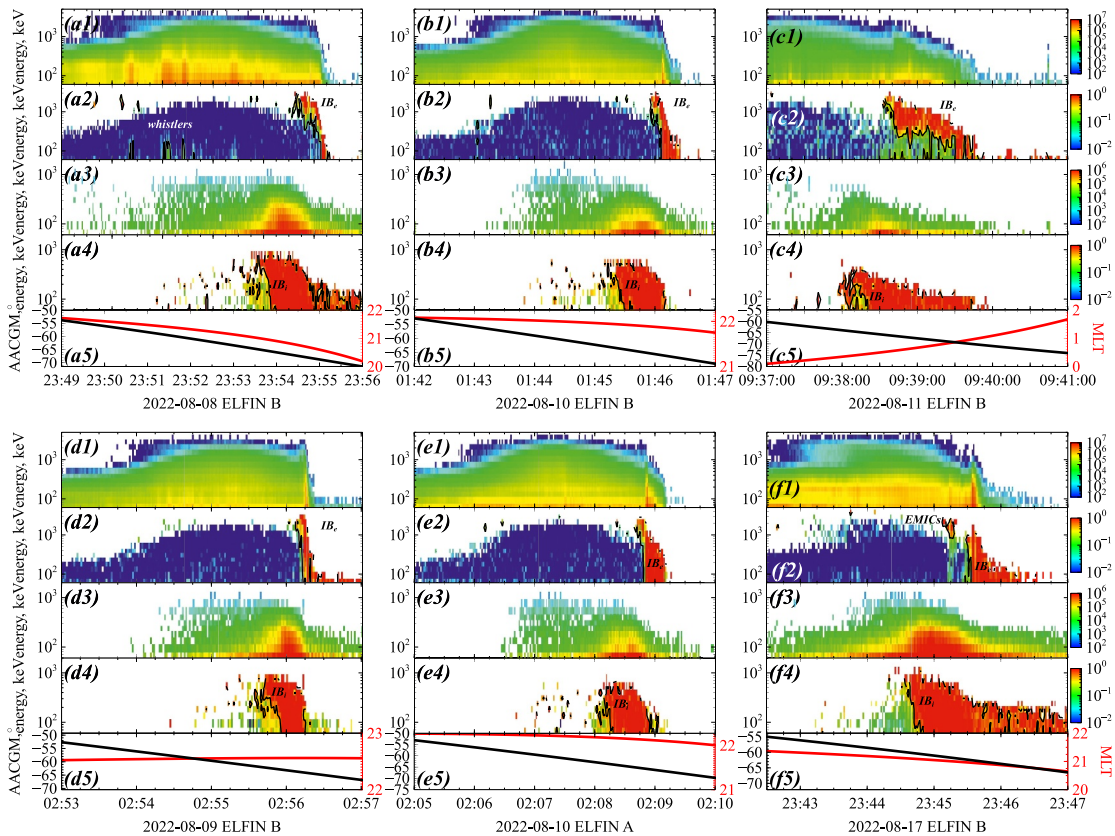


**Figure 2.** Six ELFIN orbits with simple electron and ion IB patterns. From top to bottom, each set of panels (*a–f*) shows: electron-trapped fluxes in $(cm^2\ s\ sr\ MeV)^{-1}$ (panel #1), electron precipitating-to-trapped flux ratio (panel #2), ion trapped fluxes in $(cm^2\ s\ sr\ MeV)^{-1}$ (panel #3), ion precipitating-to-trapped flux ratio (panels #4), ELFIN AACGM latitude in black and MLT in red (panel #5).

precipitation of the electrons after the time exceeding the loss time scale. The availability of energetic particles in the plasma sheet (like in events *c*, *d* and *f*) provides precipitating of <200keV electrons poleward from IBe pattern, whereas wave activity within the outer radiation belt provides sporadic precipitation burst equatorward from IBe pattern (like in events *a* and *f*) (see details of wave-driven precipitation patterns in Angelopoulos et al., 2023; Tsai et al., 2022; Zhang et al., 2022).

The dispersion slope of IBe in panels (*d*) is steeper than in cases (*a*, *b*, *c*), here it takes only a couple of satellite spins for IBe to scan from 1 to 2 MeV down to 50 keV energy. In more extreme cases, the transition occurs during only one spin (<3sec, <0.2° of latitude) at the energies spanning more than an order of magnitude (*e*, *f*), such events are reasonable to distinguish as a class of steep dispersion events, which potentially can be related to either sharp spatial gradient of the equatorial quasi-static magnetic field or sharp field gradients in mesoscale transient structures. It is of note that the proton isotropy boundary (IBp) does not show any related difference in Figure 2 (panels #4), and the IBp pattern is systematically located $1 - 2°$ equatorward of the IBe pattern location, which is quite typical (e.g., Sergeev et al., 2012; Shevchenko et al., 2010). IBp pattern covers the energy range from the plasma sheet energetic ion population (below ~200keV) and up to the most energetic part of the ring current, ~1MeV (e.g., Gkioulidou et al., 2016; Yue et al., 2017). All events shown in Figure 2 occurred in nearly quiet AE condition, with two events (*a*, *f*) occurring at the end of substorm recovery and one event (*c*) at the very beginning of substorm growth phase.

An important category of the IB dispersion includes a non-monotonic variation of threshold energy with magnetic latitude (remember that $E_c$ corresponds to a jump from red to green at each vertical slice). Figure 3 shows six examples of non-monotonic IBe patterns. The most widespread type is the IBe pattern with an inserted gap of energetic electron (<300keV) precipitation (examples *b*, *c*, *d*). Such gaps have different latitudinal extents (generally a few ELFIN spins) and can be observed single (*b*, *d*) or as a group (*c*, *e*, *f*). Each of these precipitation

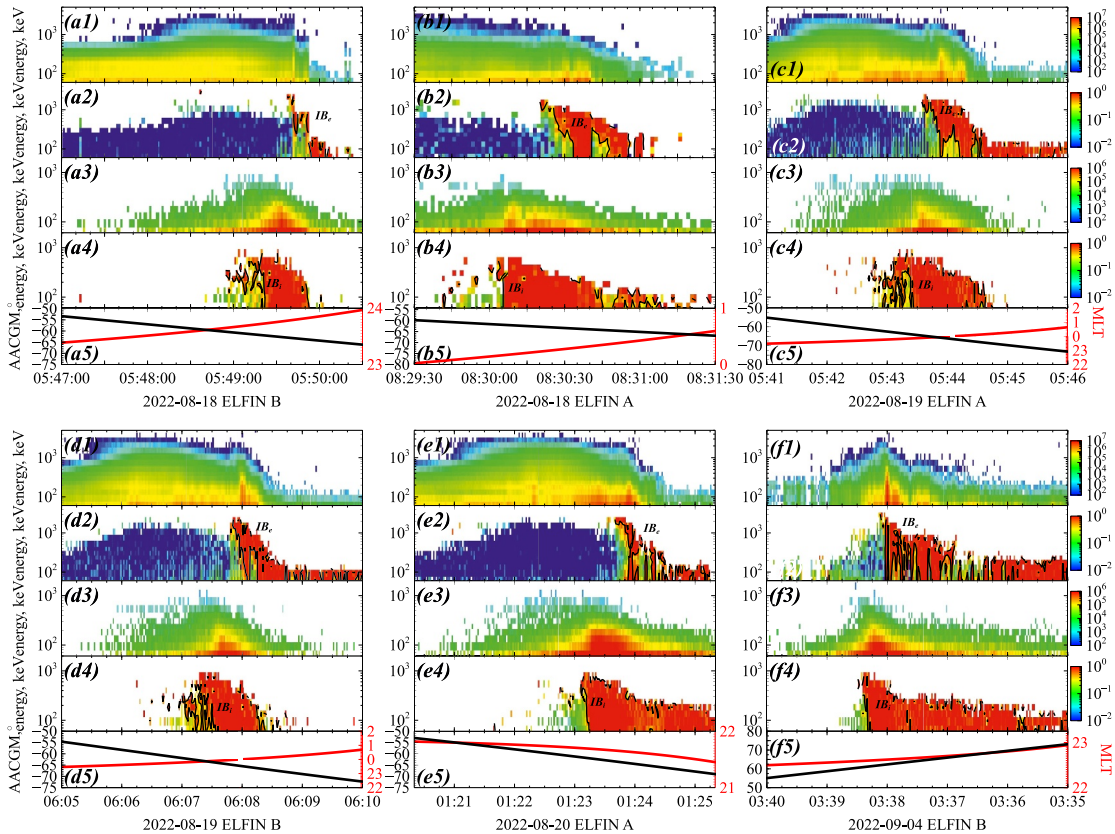


**Figure 3.** Same as in Figure 2 but for events showing non-monotonic IB pattern.

gaps can be interpreted as a local enhancement of the equatorial magnetic field or a decrease of the current density, which increases the curvature radius and suppresses the precipitation (see details in Discussion). Two examples in Figure 3, (*a*, *e*) show more complicated non-monotonic IBe patterns, in which the high energy part of precipitation is fragmented (but still follows general energy/latitudinal dispersion), whereas low-energy part of precipitation is variable and sometimes look intermittent, like in event (*f*). AE activity was not much different compared to events in Figure 2: the traversals in Figure 3 occurred in quiet conditions (*a*, *b*, *d*), during the substorm recovery (*e*, *f*) or just after it (*c*).

Besides the FLCS-type, which routinely provides isotropic electron precipitation from ORB to plasma sheet transition near midnight (e.g., Wilkins et al., 2023), other mechanisms contributing to isotropic precipitation can sometimes be clearly discerned in the nearby region. Figure 4 shows six examples of such precipitation patterns. In all examples we deal with the whistler-mode driven electron precipitation characterized by isotropic precipitation bursts at low energies (tens to hundred keV) with anisotropic ($R \ll 1$) loss cone distributions at high energies which show $R = j_{prec}/j_{trap}$ ratio decrease with the energy increase (see detailed analysis of such events in Tsai et al., 2022; Artemyev, Neishtadt, & Angelopoulos, 2022). Figures 4b and 4f (~13:56:20UT) show examples where ELFIN sees strong bursty isotropic precipitation of low energy (<300keV) electrons scattered by whistler-mode waves in the absence of FLCS type precipitation at high energies. In Figures 4a–4e both types (FLCS and WIP) of isotropic precipitation are observed and they are easily distinguished on ELFIN energy-time electron diagrams (panels #2); here low-energy whistler-produced precipitations start well equatorward of FLCS precipitation (*a*, *c*, *d*, *e*), sometimes even equatorward of the proton IB (e.g., event (*b*)). Different from previous examples in Figures 2 and 3, these events are associated with the clear AE signatures of substorm activity, including either expansion (events *b*, *c*, *d*) or recovery phase (*f*) of an intense substorm, or pseudobreakup range activations (*a*, *e*).

These events are expected to be associated with substorm electron injections that penetrate into the outer radiation belt and bring hot anisotropic electrons generating whistler-mode waves (e.g., Fu et al., 2014; Tao et al., 2011). The upper energy range of electron precipitation by whistler-mode waves is largely controlled by wave intensity

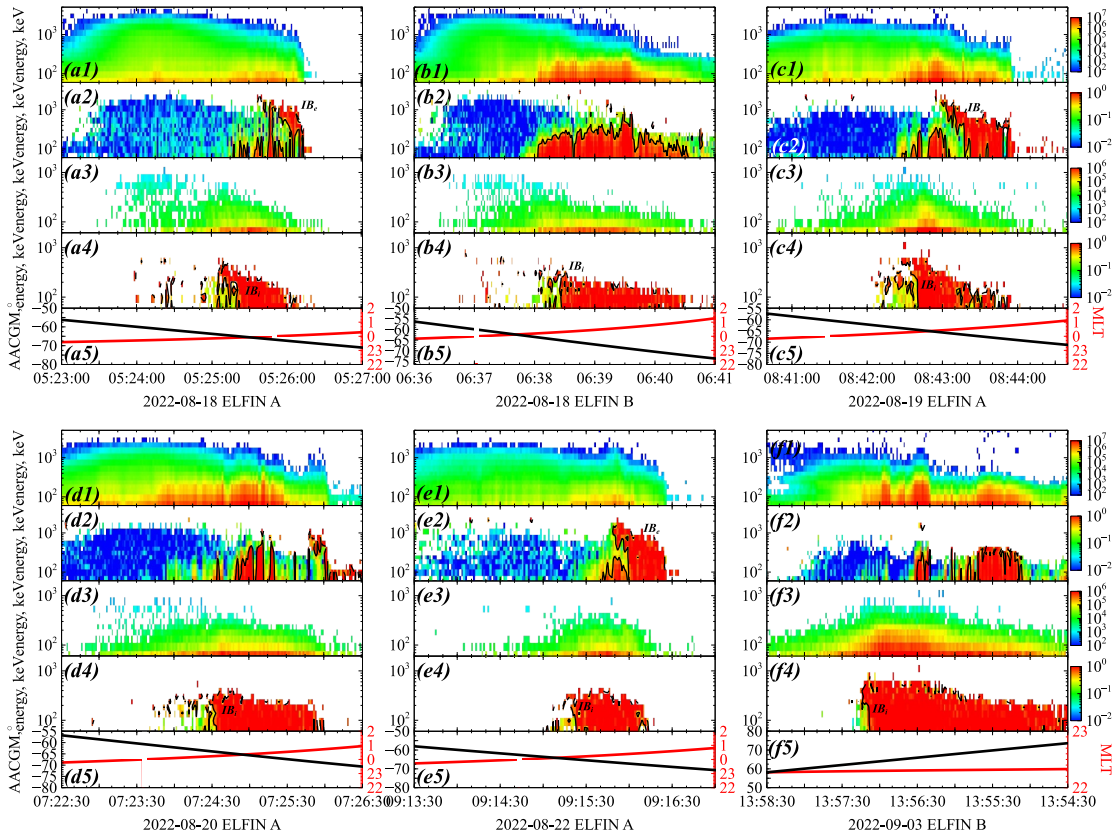


**Figure 4.** Same as in Figures 2 and 3 but for events showing whistler-mode driven precipitation pattern observed together with (a, *c-f*) or without (b) the FLCS-type isotropic precipitation.

spread along magnetic field lines (see discussion in Artemyev et al., 2024). The night-side whistler-mode waves are generally confined within 20° of magnetic latitude (e.g., Agapitov et al., 2018; Meredith et al., 2012), which corresponds to scattering and precipitation of sub-relativistic (<500keV) electrons (e.g., Summers, 2005). This limitation of the upper energy range helps to distinguish whistler-driven and FLCS precipitation: the former provides precipitation bursts with $R \approx 1$ below the low-latitude edge of the IBe pattern (see *a*, *c*, *e*). Such a complex picture combining whistler-driven precipitation at low energies and FLCS-driven precipitation at high energies with the precipitation gap at intermediate energies cannot be recognized reliably using sparse energy coverage from POES observations.

To summarize this section, we list main categories of IB patterns that can be found in ELFIN dataset. The first category includes simple monotonic IB patterns that are produced by FLCS and do not include WPI effects. This category overlaps, but not fully, with the second category of specific type of IB patterns having almost dispersionless structure (very steep IB). Such steep IB may be overlap with precipitations due to WPI. The third category of IB patterns includes events with non-mononotic IB having multiple significant dropouts of *R* ratio. The fourth category consists in IB patters having inverse dispersion and likely produced by precipitations due to WPI. More detailed discussion and percetange of these categories are provided in Section 5.

## 4. ELFIN/POES Comparison of IB Patterns

In this section, we provide detailed comparisons of ELFIN and POES measurements for several orbits in which both satellites cross IBe almost simultaneously and with a small MLT separation. This allows us to compare different ways of IB identification and pattern categorization, compare its locations and get impression concerning stability of IBe structures on the spatial scale of several hundreds km and temporal scale of a few minutes.

During the first event (Figure 5) occurred during quiet period, both spacecraft observed a compact (less than 1° latitude wide) intense isotropic electron precipitation pattern. It occurred at the sharp Outer Radiation Belt (ORB)

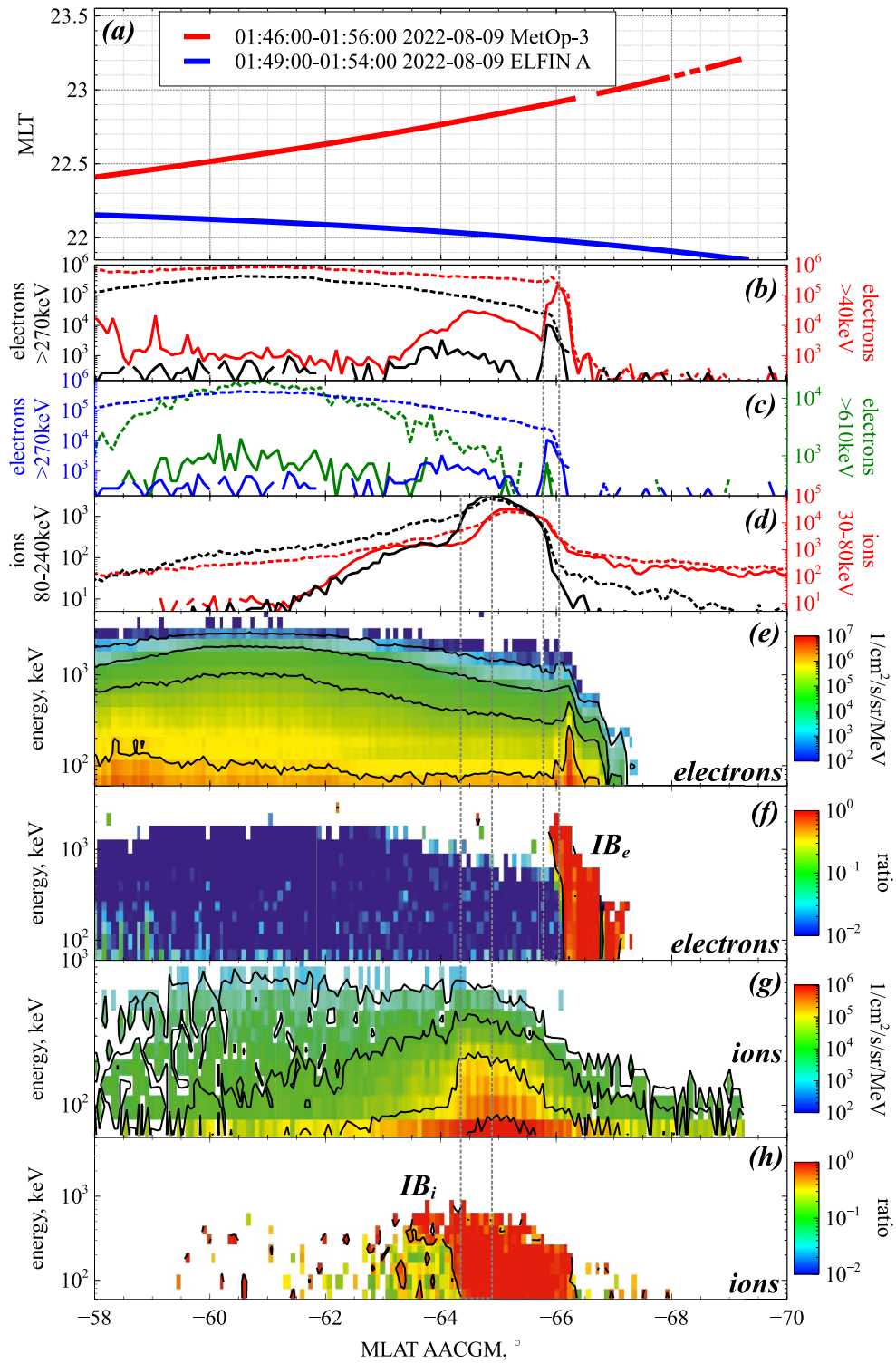


**Figure 5.** An example of ELFIN/POES(MetOp-3) comparison on 9 August 2022: (a) spacecraft orbits in MLT, MLAT plane (time is indicated in the legend) (b), (c) POES electron precipitating (solid lines) and trapped (dashed lines) fluxes for four integral channels in $(cm^2\ s\ sr)^{-1}$, (d) POES proton precipitating (solid lines) and trapped (dashed lines) differential fluxes for two channels in $(cm^2\ s\ sr\ keV)^{-1}$, (e) ELFIN trapped electron fluxes, (f) ELFIN precipitating-to-trapped electron fluxes, (g) ELFIN trapped ion fluxes, (h) ELFIN precipitating-to-trapped ion fluxes.

edge at around 66° AACGLat, according to POES observations the polar auroral precipitation boundary was at ∼73° AACGLat. This *classic* IBe pattern has a FLCS-type dispersion at high energies above 300 keV (consistent with more earthward location of IBe in 270 and 610 keV POES channels); However, it is rather steep at low energies (consistent with simultaneous IBe recordings in 40 and 130 keV POES channels, not shown here). Proton IB is also consistent at two spacecraft, being about $1.5 - 2°$ equatorward of IBe location. This quiet-time event illustrates how ELFIN and POES record the same structure and can provide similar identification of the IBe patterns during simple events.

The second event (Figure 6) took place in the recovery phase (AE above 500 nT) of small storm with the Dst peak below −50nT, which explains unusually small IBe latitude, at about 62° AACGMLat. The local time difference is substantial between ELFIN and POES (∼3hrs MLT); nevertheless the recorded IB latitudes are similar for both electrons (compare panels *b*, *c* and *f*) and protons (*d* and *h*), with IBp being about 1° equatorward of IBe. There are couple important details to notice. First, in the post-midnight sector at energies below ∼200keV ELFIN observed whistler-driven precipitation burst right equatorward of IBe, which has no analogous counterpart in POES data (this is possibly explained by MLT differences of observations). Second, poleward from IBe POES shows two localized depletions of precipitating 40 keV electron fluxes, marked by black arrows in panel *b*. Comparison with ELFIN (panel *f*) shows that similar electron flux depletions are indeed observed at several energy channels without associated changes of both trapped population (panels *e* and *g*) and proton precipitation (*h*). Being observed at the points separated by 3 h of MLT in the magnetotail, these structures probably provide an example of relatively large-scale ridge-like equatorial magnetic field enhancements in the midtail plasma sheet (see Sergeev et al., 2018; Sitnov, Stephens, et al., 2019).

The third event (Figure 7) occurred during the early substorm growth phase which started at weakly disturbed background, ∼200nT AE in association with southward IMF $B_z$ of −3nT. Consideration of POES data alone provides somewhat confusing results. Although proton IB is registered at ∼65°AACGMLat, the isotropic electrons did not appear until ∼68°, showcasing it being observed in the region of weak fluxes at the very edge of outer radiation belt. In between these latitudes, the POES electron detectors (panels *b*, *c*) registered anisotropic precipitation with larger precipitated-to-trapped flux ratio seen at lower energies. Sensitive and high-resolution ELFIN data are mutually consistent with POES description and explain how whistler-driven low-energy isotropic precipitation bursts are seen above ∼65° latitude and they are overlapped in latitude with FLCS-produced MeV electron precipitation above 66° (largely missed by sparse POES observations). This event is more complicated than previous two, and it clearly shows an advantage of ELFIN-based pattern analyses in distinguishing isotropic energy components of different origin and pattern categorization.

The fourth event (Figure 8) occurred under similar conditions during the same day and at the very beginning of the growth phase of (eventually) intense substorm. Consideration of POES data alone provided confusing results: a broad region (between 67° and 69°) of isotropic precipitation is observed in >270 keV electron channel (blue traces in third panel from top) at the ORB outer boundary in the absence of similar feature in low energy channels (see second panel). This nicely corresponds to broad plateau region of high-energy isotropic precipitation at energies, roughly, above 300 keV seen in the sixth panel. This agreement possibly indicates a relatively large-scale $B_z$ plateau region in the magnetosphere. Instead, two low energy POES channels (>40 and >130keV) demonstrate small-scale increases of isotropic precipitation centered at ∼67.5° and 68.6° which are not seen at ELFIN. A more wide spike of isotropic precipitation is seen at low energy by both spacecraft at ∼69.5° but with different appearance features. At ELFIN, the isotropy is seen at all energies, yet in the >40keV channel it is seen without accompanying isotropic fluxes in >130keV channel at POES. Therefore, this observations are excluding FLCS interpretation of low-energy spike in this area. Again, this complicated event shows a general agreement between two spacecraft/instruments (also in the location of proton IB at ∼65.3° latitude) with embedded small-scale (or transient) features. It also demonstrates an advantage of ELFIN observations in the pattern categorization in complex events.

Summarizing, the comparison of POES and ELFIN measurements shown in Figures 5–8 demonstrates that ELFIN electron measurements confirm the interpretation of IBe location and structure derived from POES measurements for simple IBe patterns. The similarity is also observed for IBp detected by ELFIN and POES. Being observed at the spacecraft with $\sim 1 - 2$h MLT spatial and a few minutes temporal separation, this indicates a relatively large scales of these IBe patterns. However, more complex phenomena such as non-monotonic IBe

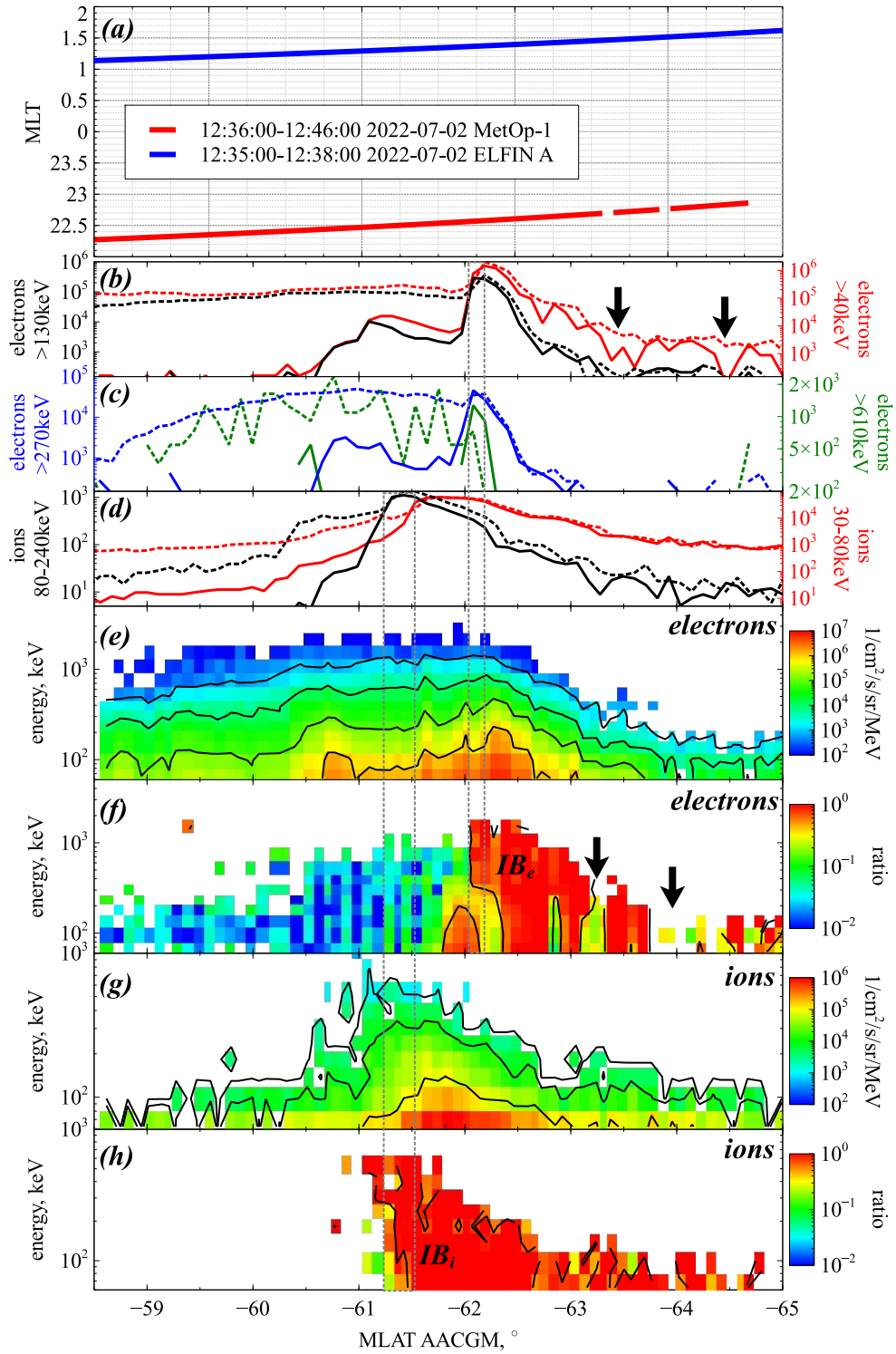


**Figure 6.** Same as in Figure 5 for ELFIN/POES(MetOp-1) comparison on 02 July 2022.

patterns, mixture of FLCS and whistler-driven scattering, and precipitation depletion in the plasma sheets are much better resolved and easily interpreted with ELFIN measurements. Therefore, such comparison can help in interpretation of much larger POES dataset, knowing how different precipitation patterns are observed by ELFIN and POES. We may also interpret POES-only measurements (historical and future) with much more confidence.

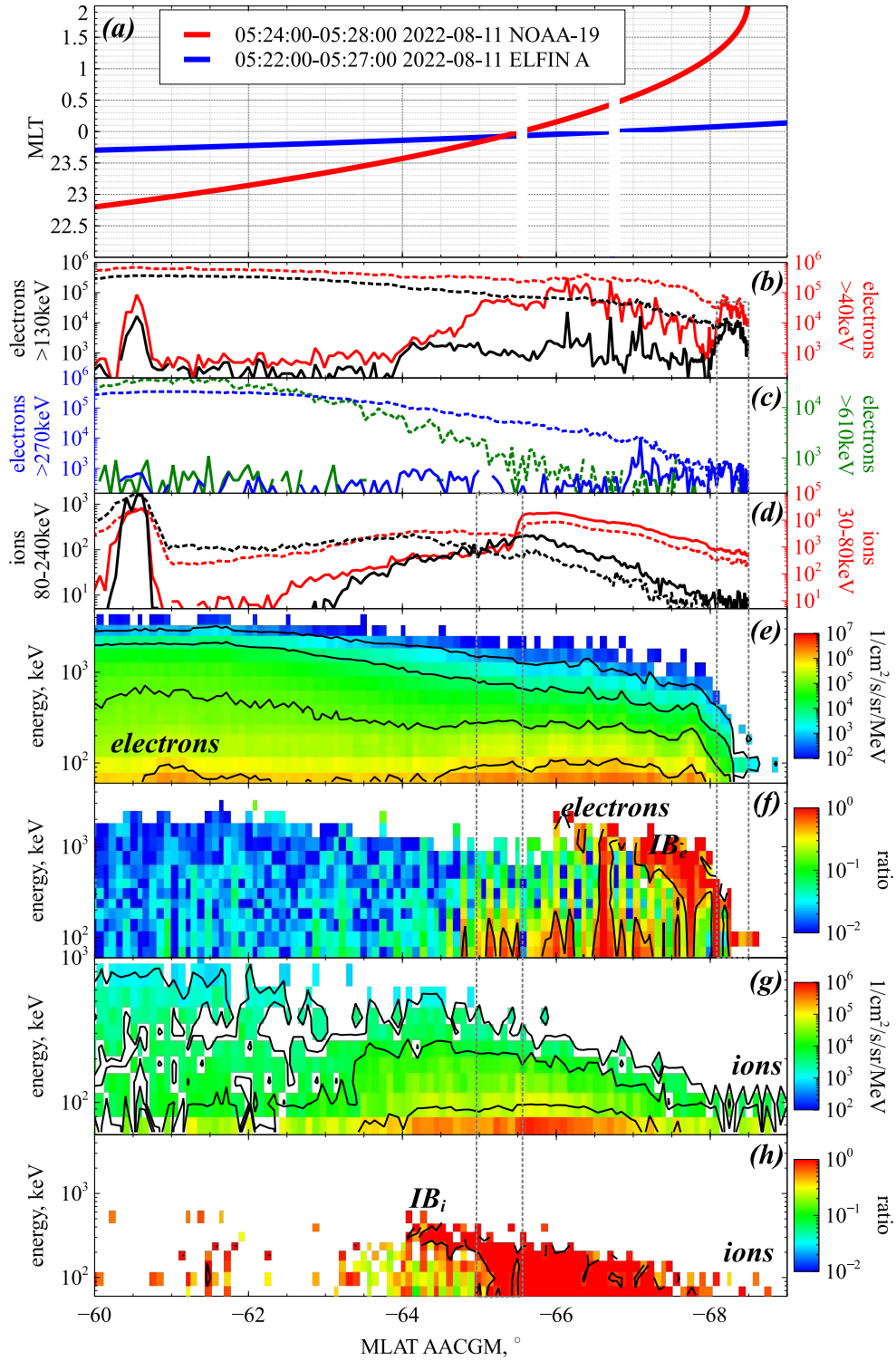


**Figure 7.** Same as in Figure 5 for ELFIN/POES(NOAA-19) comparison on 11 August 2022.

## 5. Statistical Overview

Here we briefly characterize the occurrence of different categories based on the limited statistics available from 2 month of ELFIN observations in order to give a hint of their relative occurrence. Altogether, for nearly 2 months (July–September 2022) we've had 87 auroral zone crossings in the 21-03 MLT sector. From them in 25 cases, the

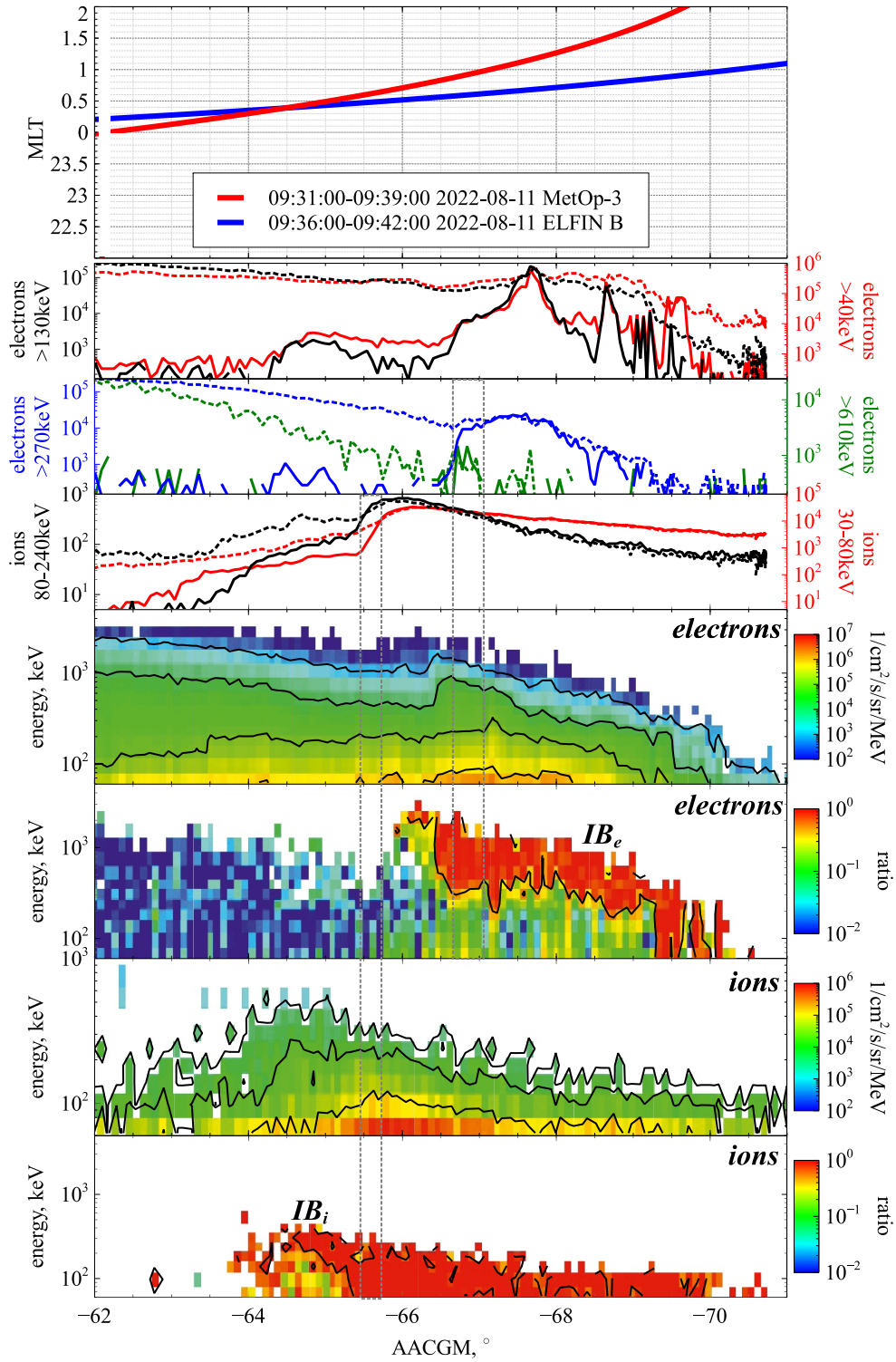


**Figure 8.** Same as in Figure 5 for ELFIN/POES(METOP-3) comparison on 11 August 2022s.

FLSC isotropic precipitation was not detected; in most cases no *red regions* of high-energy isotropic precipitation at the outer ORB edge is seen in the presence of low-energy whistler-produced precipitation (like in Figure 4b) or without such precipitation (not shown here). Most of such cases appear in the quiet conditions or during substorm recovery phase, probably due to dipolarized magnetic configuration in near-Earth tail existing during these times.

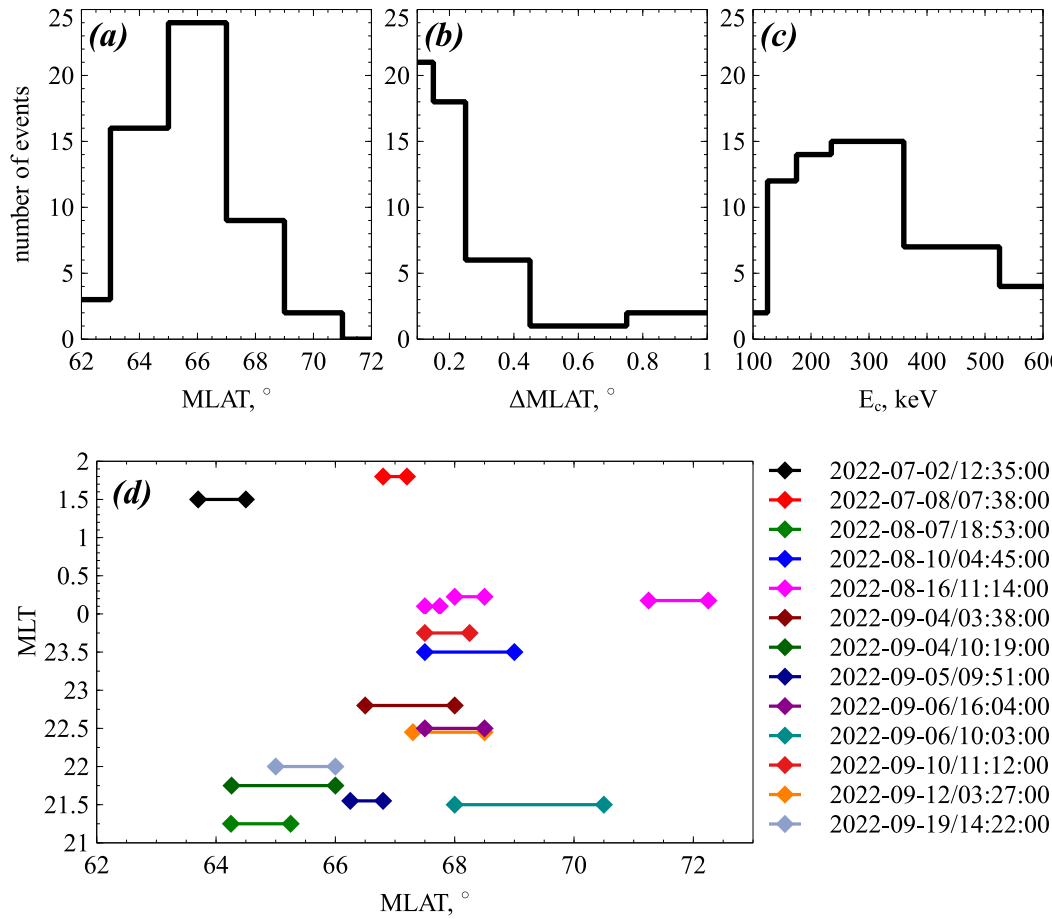


**Figure 9.** Statistical properties of non-monotonic IBe and precipitation dips poleward from IBe. Panels (a)–(c) show distributions of characteristics of 54 partial depletions of energetic electron precipitation embedded within IBe. Each depletion is characterized by MLAT (a), width of MLAT (b), and upper energy $E_c$ (c). Panel (d) shows MLAT versus MLT distribution of precipitation dips observed poleward from IBe. There are 16 such dips, and three of them are observed for the same ELFIN orbit (14 separated events).

Below the relative occurrence is referred to the remaining 62 cases as well as to total amount of 87 events (given in parentheses). Note that many categories do not exclude each other, so formally the IBe pattern can be categorized as steep and multiple (or monotonic and steep, etc.) at the same time.

The most simple FLCS-type monotonic dispersion events (see Figure 2) are observed roughly in one third, in 32% (23%). The steep dispersion cases which had nearly coinciding IBs at multiple energies (like Figures 2b and 3a–3c, 3f, Figures 4c and 4d) are also pretty frequent, and are observed in 45% (32%) cases. The structured precipitation (multiple IBs) with two or more significant $R = J_0/J_{90}$ dropouts (like those in Figures 3b–3d, 3e, 3f, Figure 4) presents 26% (18%). Finally the clear reversed (wave-induced) dispersion patterns (check again) are observed in 18% (12%) of all crossings.

To characterize the properties of precipitation dips poleward from IBe giving rise to multiple IBe occurrence, Figures 9a–9c shows distributions of parameters of 54 partial precipitation depletions embedded into IBe patterns. We use following criteria for selection of depletions: poleward and equatorward boundaries of depletion have $j_{prec}/j_{trap} \approx 1$ at 50 keV channel. The depletion shows $j_{prec}/j_{trap} < 0.5$,and this threshold determines upper energy boundary, $E_c$. Magnetic latitudes of these depletions (Figure 9a) cover the typical IBe latitude range (Wilkins et al., 2023). The time resolution of ELFIN measurements is 3 s, and this is approximately 0.1° of MLAT for this latitude range. A significant fraction of observed depletions has this spin-resolution ΔMLAT size, but there are also depletions with ΔMLAT≈ 0.3° and larger (panel (*b*)). Typical upper energy for such depletion, $E_c$, is within

[150,400]keV range. Note, all depletions have $j_{prec}/j_{trap} \approx 1$ at the polarward and equatorward boundaries for 50 keV energy channel.

Panel *d* shows MLAT, MLT distribution of another type of precipitation dips observed poleward from IBe. There are 16 such dips, and three of them are observed for the same ELFIN orbit (14 separated events). Each of the dips are characterized by: $j_{prec}/j_{trap}$ below 0.5 (often $j_{prec}/j_{trap} \approx 0$) for all energies, large $j_{prec}$ for ions (i.e., this is electron precipitation dip), clear MLAT boundaries with $j_{prec}/j_{trap} \approx 1$ for electrons, and a polwerward location relative to IBe (within the plasma sheet or in the outer edge of the transition region). All dips are observed within 5° of MLAT from IBe, and most of dips (except three) are within 3° of MLAT from IBe. Figure 8d shows MLT, MLAT distribution of such dips. Most of them have a spatial scale of ΔMLAT<2°. In projection to the equatorial plane this scale will be $\Delta r < 3.5R_E$ (see Discussion section for ΔMLAT→ $\Delta r$ transformation details).

## 6. Discussion and Concluding Remarks

Determination of true FLCS boundary, used to be determined by the reconstruction of the equatorial magnetic field profile based on low-altitude observations. This is the major goal of the IB pattern studies. Therefore, it is convenient to start discussion by considering theoretical FLCS-related IB patterns expected from the data-based average magnetospheric models. Figure 10 provides example calculations for low- and modestly disturbed ($Kp = 1$ and 3) T89 models (Tsyganenko, 1989), as well as for recent TA15 model (Tsyganenko & Andreeva, 2015). The latter case includes three examples ranging from quiet conditions (northward IMF $B_z$, Newell index $FN = 0.11$) to disturbed conditions (southward $B_z \sim -4$nT, $FN = 1.35$). All calculations are done in the midnight meridian plane under zero dipole tilt. Here we show the ionospheric footpoint AACGM latitude, equatorial parameters $(r, B_z)$, and critical rigidity ($G = mV/e$, where $V$ is the particle velocity) at which the IB is formed at the given magnetic field line. These parameters are computed at the model's equator (where $B_x = 0$) as $G_c = B_z^2/(8dBx/dz)$. The particle energies corresponding to these critical rigidities are cross-referenced in Figure 10c.

The simulated IB patterns in the ionosphere shown in Figure 10a confirm the expected latitude-energy ($G$)-dependence and are roughly consistent between simplest (T89) and more advanced (TA15) models. The IB latitude for ~100keV electrons $(G \sim 0.2\text{nT} \cdot R_E)$ vary between $65 - 68°$ at midnight, which is consistent with typical IBe locations (Wilkins et al., 2023) and with examples given in Figures 2–4. However, the profiles from recent (more sophisticated and based on much larger data set) TA15 model demonstrate the plateau-like $B_z(r)$ features near the inner edge of tail current sheet with associated plateau-like piece of IB pattern, which qualitatively resemble the ELFIN observations in Figure 8. Even the average models demonstrate the IB patterns with varying slopes and some non-monotonic non-standard features (see more examples in Shi et al., 2024).

To convert the latitudinal scale-sizes of IB features ($\Delta X_i$) to their radial scale-sizes in the equatorial plane ($\Delta X_m$), one may use the magnetic flux conservation in the flux tube with rectangular cross-section in the ionosphere ($\Delta X_i, \Delta Y_i$) and magnetosphere ($\Delta X_m, \Delta Y_m$) in the form $\Delta X_i B_i \Delta Y_i = \Delta X_m B_m \Delta Y_m$. Here, magnetic field magnitudes are $B_i = 50000$nT in the ionosphere, and equatorial $B_m \sim 15$ nT correspond to the magnetic field $B_z$ amplitude evaluated from the threshold of isotropic scattering FLCS (for energy $E = 100$keV). From this, by denoting $F_Y = \Delta Y_m/\Delta Y_i$ we have for rough estimates

$$\Delta X_m[\mathrm{R_E}] = \Delta X_i \cdot (B_i/B_m)/F_Y \sim \Delta X_i[100\mathrm{km}] \cdot 1.74$$

Here, we used a characteristic value $F_Y \sim 30$ which follows from model computations shown in Figure 9c for $G_{cr}$ in the range $0.2 - 0.6\text{nT} \cdot R_E$ corresponding to energies $E \sim 100 - 300$keV. For example, the minimal size that can be resolved by ELFIN spectrograms in the IB patterns corresponds to its 3 s spin resolution (0.2° latitude), which gives roughly about $0.35R_E$ which is well above the ion scale-size in the plasma sheet.

Previously, a number of various magnetic features in the near-Earth equatorial magnetotail were reported from magnetospheric spacecraft observations or numerical simulations. This can potentially contribute to formation of the non-monotonic IB profile features. They encompases the mesoscale range $B_z$ minimum features during the growth phase-type conditions (Sergeev et al., 2018; Sorathia et al., 2020; Yang et al., 2014), large-amplitude turbulent dipolarization regions during the substorm expansions (e.g., Ohtani et al., 1998), as well as sub-ion scale magnetic holes (Shustov et al., 2019; Zhang et al., 2017) and Earthward-propagating dipolarization

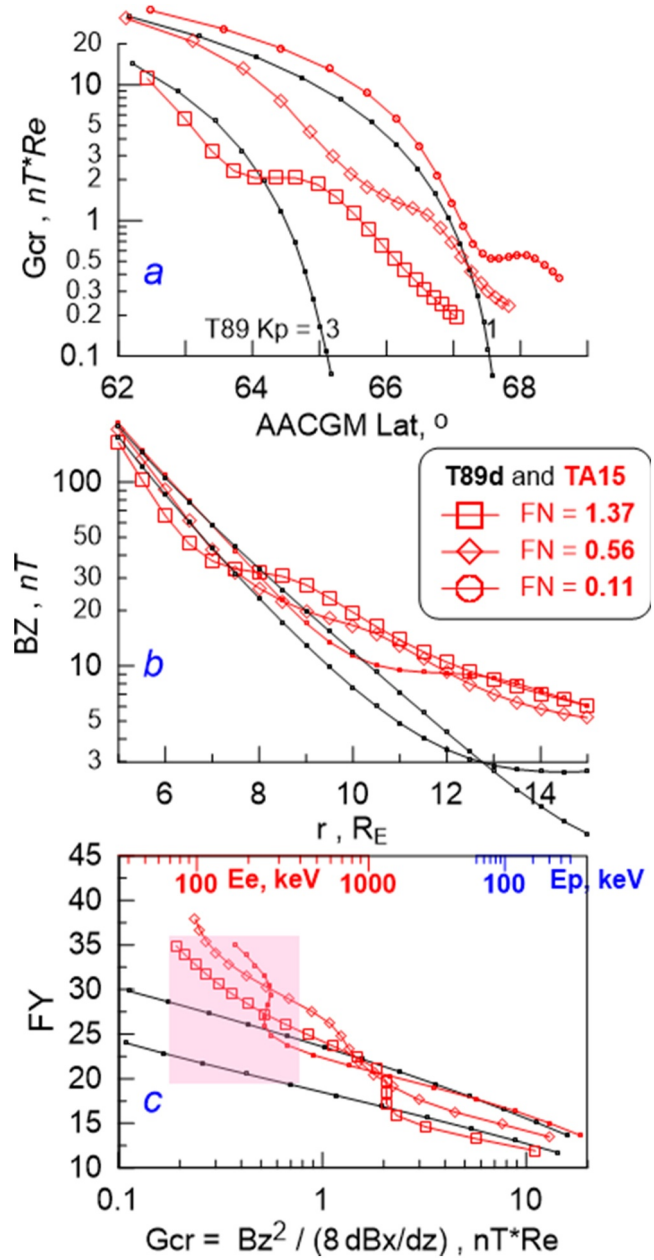


**Figure 10.** Some characteristics of theoretic IB pattern for zero dipole tilt in the midnight meridional plane according to empirical models by Tsyganenko (1989) and Andreeva and Tsyganenko (2016). From top to bottom: (a) theoretical IB pattern showing the dependence of critical rigidity $G_{cr}$ against the footpoint latitude of IB field line; (b) equatorial $B_z$ against radial distance of IB field line; (c) mapping factor FY against critical rigidity.

fronts (Sergeev et al., 2009), see also a summary of transient features in the magnetotail in (Sharma et al., 2008; Sitnov, Birn, et al., 2019). Below we briefly discuss which properties of magnetic terrain $\left(B_z(r)\right)$ features can be inferred from interpreting different kinds of non-monotonic structures in terms of FLCS mechanism.

### 6.1. Non-Monotonic IBe Features

Although non-monotonic structure of IBe pattern can have various forms (see examples in Figure 3), the focus should be on the localized in-latitude partial depletion of electron precipitation ($R \ll 1$) at energies below an upper energy boundary $E_c$, with isotropic precipitation ($R \approx 1$) in the entire energy range (>50keV electrons). These are existing poleward and equatorward from this partial depletion region as well as at energies $E > E_c$ in the partial

depletion itself. A primeexample is given at −62.9° AACGLat in Figure 6. Statistics for this type features is given in Figures 9a–9c. Typical $E_c$ —according to the statistics— (Figure 9c) peak around 200 − 300 keV,and their frequency drops down at larger energies. The key scattering parameter, electron gyroradius to the magnetic field line curvature radius, provides the following scaling between the electron energy $E_c$, equatorial magnetic field, $B_{eq}$, and current density, $j_{eq}$:

$$\sqrt{E_c \cdot (E_c + 1022\text{keV})} \propto B_{eq}^2 / j_{eq}$$

Therefore, to suppress precipitation of <300keV electrons within a localized depletion (with $E_c = 300$keV), but keep precipitation of ∼50keV electrons within the strong diffusion limit nearby of this region ($E_c < 50$keV), we should provide $B_{eq}^2/j_{eq}$ variation of about $\sim(1.23 \cdot 300/50)^{1/2} \approx 2.75$. For constant $j_{eq}$, this variation means $\delta B_{eq}/B_{eq} \approx 0.65$. For a typical $B_{eq} < [10, 20]$nT near the IBe in the plasma sheet-inner magnetosphere transition region (Artemyev et al., 2016; Sergeev et al., 2011), we obtain the necessary variation about $\delta B_{eq} \approx 5 - 10$nT. Such variation can easily be provided by many types of localized magnetic features in the magnetotail mentioned above (see detailed investigation in Shi et al., 2024). As regards its radial scale, most of such cases are seen during only one-two spins, therefore the dominant radial scale located within 0.5° of MLAT poleward from IBe -size of magnetic variation is several tenths of $R_E$. Strong precipitation of protons is not altered in the partial depletions of isotropic electron precipitation.

### 6.2. Precipitation Dips Poleward From IBe

Examples of such complete precipitation dips are marked by arrows in Figure 6f, and locations of 16 such dips found within 5° of MLAT poleward from IBe are plotted in Figure 9d. For the first depletion of electron precipitation (around 63.2°, Figure 6f), the ratio $j_{prec}/j_{trap}$ drops to ∼0.3 (yellow instead of red) that is, FLCS mechanism should still operate near the threshold. For the second depletion, all precipitating fluxes disappear despite the trapped electrons containing energies up to 200 keV (i.e., this magnetic field enhancement is large in its both amplitude and radial scale). Isotropic precipitation of protons are not affected in these regions as well. Such dropouts, similarly to the partial depletions of IBe patterns considered in above, should be associated with enhancements of the equatorial magnetic field (see discussion in Sergeev et al., 2018; Shen et al., 2023). These enhancements are expected to be of larger scaler and more steady (see discussion in Sitnov, Stephens, et al., 2019; Stephens et al., 2019); this is confirmed by their recordings made at each of ELFIN and POES spacecraft separated by ∼3hrs MLT. Most of 16 dips of electron precipitation have a spatial scale of Δ MLAT≈ [0.5°, 1°], so they would correspond to a few $R_E$ size in the radial direction.

### 6.3. Whistler-Driven Precipitation

Overlapping of IBe and whistler-driven precipitations provides a trouble for determination of the true FLCS boundary location. When observed alone (e.g., Figures 4b and 4d), the whistler-mode scattering occupies the lower-part of ELFIN energy spectrogram. When two mechanisms can be identified simultaneously, the ELFIN observes the FLCS-related relativistic electrons (above 500 keV) simultaneously with whistler-mode scattering of energetic electrons (below 300 keV), often showing a precipitation drop at intermediate energies (see examples in Figures 3e and 4a, 4c and 4e, Figures 6f and 7f). So, when both mechanisms operate at these times, their effects often can be distinguished/separated and interpreted properly.

Whistler-mode wave generation requires significant perpendicular anisotropy of <50keV electron population (Fu et al., 2014; Tao et al., 2011) which can be effectively generated mainly in strong magnetic field as a consequence of betatron acceleration. Such strong equatorial magnetic field exists in the flux tubes located earthward from IBe, which itself serves as a demarcation boundary between strong and weak equatorial $B_{eq}$ regions. In the nightside inner magnetosphere a significant fraction of the suprathermal electrons (<1keV) may quickly damp waves becoming oblique in off-equatorial region (see discussion in Artemyev & Mourenas, 2020), which results in whistler-mode wave confining around the equator, below 15° (e.g., Agapitov et al., 2013; Meredith et al., 2012). The field-aligned near-equatorial whistler-mode waves may not resonate with relativistic electrons because the resonant latitude increases with the energy increase and reaches 30° for relativistic energies (see discussion in Artemyev et al., 2024). Therefore, we generally expect that whistler-driven precipitations of nonrelativistic electrons occur at the latitudes equatorward from the 50 keV IBe. This explains some overlapping of such

precipitations with the isotropic relativistic electron fluxes within IBe pattern. Without a good energy resolution, such as provided by ELFIN, or better, this overlapping cannot be measured well and likely would result in misinterpretation of structure of such IBe pattern.

### 6.4. EMIC-Driven Precipitation

Intense EMIC waves, another long-known contributor to relativistic electron precipitation (e.g., R. Millan & Thorne, 2007; Thorne et al., 2021, and references therein), are normally observed on the dusk side in the plasmasphere and rarely occur in nearmidnight (21-02 MLT) sector occupied by FLCS precipitations (see recent review by Angelopoulos et al., 2023). Relativistic electron scattering by electromagnetic ion cyclotron (EMIC) waves may significantly complicate interpretation of the equatorward side of IBe at MeV energies. The EMIC waves generated by injected ions precipitate >500keV electrons slightly earthward from the geostationary orbit (Capannolo et al., 2023; Yahnin et al., 2017), and such precipitation may overlap with the equatorward side of IBe. In ELFIN observation this effect looks like a long almost dispersionless prolongation of >500keV isotropic precipitation equatorward from the main IBe, and this precipitation pattern mask the equatorward edge of IBe (see examples in Figure 3 (*b2*, small red patch), Figures 7 and 8f and discussion in Artemyev et al. (2023)).

### 6.5. Summarizing the Results

In this study we consider ELFIN observations of electron IB patterns and propose existence of four main (but overlapping) categories of such patters: the first category (32%) includes events with simple monotonic IBs, the second category (45%) includes events with steep dispersion (almost dispersionless) IBs, the third category (26%) includes events with structured (non-monotonic) IBs, the fourth category (18%) includes events with reversed dispersion of IBs. We emphasize the following findings about these four categories.

- Sensitive high energy-resolution electron flux measurements in the wide energy range (tens keV to a few MeV) with loss-cone control provided by ELFIN EPD instrument are important to characterize the IBe patterns in near-midnight MLT sector and distinguish the FLCS precipitation from wave-induced contributions. A general agreement between ELFIN and POES simultaneous nearby observations indicate a relatively large-scale nature of the inferred IBe patterns.
- Large amounts (up to 2/3 of all events) of non-monotonic—or steep, sometimes multiple—IBe patterns suggest abundance of non-trivial tail current sheet structures, or the mixed contribution of two mechanisms in vicinity of the IBe in these cases. Further investigations of these IBe patterns measured with high sensitivity and resolution are supported by in situ magnetospheric observations are important to identify true FLCS boundary (ies) and use them to investigate the variable dynamical magnetospheric configuration of the transition from plasma sheet to the radiation belt.
- Sensitive high energy-resolution electron flux measurements in the wide energy range (tens keV to a few MeV) and loss-cone pitch angle resolution are important to distinguish/separate the contributions of FLCS precipitation from wave-induced intense precipitation. High upper energy of electron spectrometer (up to and above 1 MeV) is critical in categorizations of IBe patterns. High time resolution (down to 1 s or better) is strongly recommended to fully resolve the multiple IB structure and steep IB events, as well as to reveal bursty character of wave-induced precipitation. The possibility to follow the IBe evolution from observations of closely spaced constellations of polar spacecraft would be a great advantage of these studies.

These conclusive remarks underscore the importance of new forthcoming missions that may provide higher resolution probing of IBe structure, better equipped with a multi-spacecraft observations resolving questions about spatial scales of IBe non-monotonic features and their temporal variations (see R. Millan & Ukhorskiy, 2024; Ukhorskiy & Millan, 2024).

## Data Availability Statement

ELFIN A and B flux data is available at https://cdaweb.gsfc.nasa.gov/misc/NotesE.html#ELA_L1_EPDEF and https://cdaweb.gsfc.nasa.gov/misc/NotesE.html#ELB_L1_EPDEF. Data was retrieved and analyzed using PySPEDAS and SPEDAS, see Angelopoulos et al. (2019).

**Acknowledgments**
A.V.A., X.J.Z., and V.A. acknowledge support by NASA awards 80NSSC22K0752, 80NSSC23K0108, 80NSSC21K0729, 80NSSC24K0558 and NSF grants AGS-1242918, AGS-2019950, and AGS-2021749.We are grateful to NASA's CubeSat Launch Initiative for ELFIN's successful launch in the desired orbits. We acknowledge early support of ELFIN project by the AFOSR, under its University Nanosat Program, UNP-8 project, contract FA9453-12-D-0285, and by the California Space Grant program. We acknowledge critical contributions of numerous volunteer ELFIN team student members.

## References

Agapitov, O. V., Artemyev, A., Krasnoselskikh, V., Khotyaintsev, Y. V., Mourenas, D., Breuillard, H., et al. (2013). Statistics of whistler mode waves in the outer radiation belt: Cluster STAFF-SA measurements. *Journal of Geophysical Research*, *118*(6), 3407–3420. https://doi.org/10.1002/jgra.50312

Agapitov, O. V., Mourenas, D., Artemyev, A. V., Mozer, F. S., Hospodarsky, G., Bonnell, J., & Krasnoselskikh, V. (2018). Synthetic empirical chorus wave model from combined van allen probes and cluster statistics. *Journal of Geophysical Research (Space Physics)*, *123*(1), 297–314. https://doi.org/10.1002/2017JA024843

Andreeva, V. A., & Tsyganenko, N. A. (2016). Reconstructing the magnetosphere from data using radial basis functions. *Journal of Geophysical Research (Space Physics)*, *121*(3), 2249–2263. https://doi.org/10.1002/2015JA022242

Angelopoulos, V., Cruce, P., Drozdov, A., Grimes, E. W., Hatzigeorgiu, N., King, D. A., et al. (2019). The space physics environment data analysis system (SPEDAS). *Space Science Reviews*, *215*(1), 9. https://doi.org/10.1007/s11214-018-0576-4

Angelopoulos, V., Tsai, E., Bingley, L., Shaffer, C., Turner, D. L., Runov, A., et al. (2020). The ELFIN mission. *Space Science Reviews*, *216*(5), 103. https://doi.org/10.1007/s11214-020-00721-7

Angelopoulos, V., Zhang, X. J., Artemyev, A. V., Mourenas, D., Tsai, E., Wilkins, C., et al. (2023). Energetic electron precipitation driven by electromagnetic ion cyclotron waves from ELFIN's low altitude perspective. *Space Science Reviews*, *219*(5), 37. https://doi.org/10.1007/s11214-023-00984-w

Artemyev, A. V., Angelopoulos, V., Runov, A., & Petrukovich, A. A. (2016). Properties of current sheet thinning at x\sim 10 to 12 R_{E}. *Journal of Geophysical Research*, *121*(7), 6718–6731. https://doi.org/10.1002/2016JA022779

Artemyev, A. V., Angelopoulos, V., Zhang, X. J., Chen, L., & Runov, A. (2023). Dispersed relativistic electron precipitation patterns between the ion and electron isotropy boundaries. *Journal of Geophysical Research (Space Physics)*, *128*(12), e2023JA032200. https://doi.org/10.1029/2023JA032200

Artemyev, A. V., Angelopoulos, V., Zhang, X. J., Runov, A., Petrukovich, A., Nakamura, R., et al. (2022a). Thinning of the magnetotail current sheet inferred from low-altitude observations of energetic electrons. *Journal of Geophysical Research (Space Physics)*, *127*(10), e2022JA030705. https://doi.org/10.1029/2022JA030705

Artemyev, A. V., & Mourenas, D. (2020). On whistler mode wave relation to electron field-aligned plateau populations. *Journal of Geophysical Research (Space Physics)*, *125*(3), e27735. https://doi.org/10.1029/2019JA027735

Artemyev, A. V., Neishtadt, A. I., & Angelopoulos, V. (2022b). On the role of whistler-mode waves in electron interaction with dipolarizing flux bundles. *Journal of Geophysical Research (Space Physics)*, *127*(4), e30265. https://doi.org/10.1029/2022JA030265

Artemyev, A. V., Zhang, X. J., Demekhov, A. G., Meng, X., Angelopoulos, V., & Fedorenko, Y. V. (2024). Relativistic electron precipitation driven by mesoscale transients, inferred from ground and multi-spacecraft platforms. *Journal of Geophysical Research (Space Physics)*, *129*(2), e2023JA032287. https://doi.org/10.1029/2023JA032287

Baker, K. B., & Wing, S. (1989). A new magnetic coordinate system for conjugate studies at high latitudes. *Journal of Geophysical Research*, *94*(A7), 9139–9143. https://doi.org/10.1029/JA094iA07p09139

Bikkuzina, G. R., Sergeev, V. A., & Bösinger, T. (1998). Particle boundaries during a solar electron event. In J. Moen, A. Egeland, & M. Lockwood (Eds.), *Polar cap boundary phenomena* (pp. 355–367). Springer Netherlands. https://doi.org/10.1007/978-94-011-5214-3_27

Birmingham, T. J. (1984). Pitch angle diffusion in the Jovian magnetodisc. *Journal of Geophysical Research*, *89*(A5), 2699–2707. https://doi.org/10.1029/JA089iA05p02699

Büchner, J., & Zelenyi, L. M. (1989). Regular and chaotic charged particle motion in magnetotaillike field reversals. I - basic theory of trapped motion. *Journal of Geophysical Research*, *94*(A9), 11821–11842. https://doi.org/10.1029/JA094iA09p11821

Capannolo, L., Li, W., Ma, Q., Qin, M., Shen, X. C., Angelopoulos, V., et al. (2023). Electron precipitation observed by ELFIN using proton precipitation as a proxy for electromagnetic ion cyclotron (EMIC) waves. *Geophysical Research Letters*, *50*(21), e2023GL103519. https://doi.org/10.1029/2023GL103519

Delcourt, D. C., & Sauvaud, J. A. (1994). Plasma sheet ion energization during dipolarization events. *Journal of Geophysical Research*, *99*(A1), 97–108. https://doi.org/10.1029/93JA01895

Dubyagin, S., Ganushkina, N. Y., & Sergeev, V. (2018). Formation of 30 KeV proton isotropic boundaries during geomagnetic storms. *Journal of Geophysical Research (Space Physics)*, *123*(5), 3436–3459. https://doi.org/10.1002/2017JA024587

Evans, D. S., & Greer, M. S. (2004). Polar orbiting environmental satellite space environment monitor-2: Instrument description and archive data documentation.

Fu, X., Cowee, M. M., Friedel, R. H., Funsten, H. O., Gary, S. P., Hospodarsky, G. B., et al. (2014). Whistler anisotropy instabilities as the source of banded chorus: Van Allen Probes observations and particle-in-cell simulations. *Journal of Geophysical Research (Space Physics)*, *119*(10), 8288–8298. https://doi.org/10.1002/2014JA020364

Ganushkina, N. Y., Pulkkinen, T. I., Kubyshkina, M. V., Sergeev, V. A., Lvova, E. A., Yahnina, T. A., & Fritz, T. (2005). Proton isotropy boundaries as measured on mid- and low-altitude satellites. *Annales Geophysicae*, *23*(5), 1839–1847. https://doi.org/10.5194/angeo-23-1839-2005

Gkioulidou, M., Ukhorskiy, A. Y., Mitchell, D. G., & Lanzerotti, L. J. (2016). Storm time dynamics of ring current protons: Implications for the long-term energy budget in the inner magnetosphere. *Geophysical Research Letters*, *43*(10), 4736–4744. https://doi.org/10.1002/2016GL068013

Gvozdevsky, B. B., Sergeev, V. A., & Mursula, K. (1997). Long lasting energetic proton precipitation in the inner magnetosphere after substorms. *Journal of Geophysical Research*, *102*(A11), 24333–24338. https://doi.org/10.1029/97JA02062

Imhof, W. L., Reagan, J. B., & Gaines, E. E. (1979). Studies of the sharply defined L dependent energy threshold for isotropy at the midnight trapping boundary. *Journal of Geophysical Research*, *84*(A11), 6371–6384. https://doi.org/10.1029/JA084iA11p06371

Kasahara, S., Miyoshi, Y., Yokota, S., Kasahara, Y., Matsuda, S., Kumamoto, A., et al. (2018). Pulsating aurora from electron scattering by chorus waves. *Nature*, *554*(7692), 337–340. https://doi.org/10.1038/nature25505

Kennel, C. F. (1969). Consequences of a magnetospheric plasma. *Reviews of Geophysics and Space Physics*, *7*(1–2), 379–419. https://doi.org/10.1029/RG007i001p00379

Lvova, E. A., Sergeev, V. A., & Bagautdinova, G. R. (2005). Statistical study of the proton isotropy boundary. *Annales Geophysicae*, *23*(4), 1311–1316. https://doi.org/10.5194/angeo-23-1311-2005

Meredith, N. P., Horne, R. B., Sicard-Piet, A., Boscher, D., Yearby, K. H., Li, W., & Thorne, R. M. (2012). Global model of lower band and upper band chorus from multiple satellite observations. *Journal of Geophysical Research*, *117*(A10), 10225. https://doi.org/10.1029/2012JA017978

Millan, R., & Ukhorskiy, S. (2024). Remote-sensing magnetotail dynamics from low earth orbit with CINEMA. In *Egu general assembly conference abstracts*. https://doi.org/10.5194/egusphere-egu24-4783.4783

Millan, R. M., & Thorne, R. M. (2007). Review of radiation belt relativistic electron losses. *Journal of Atmospheric and Solar-Terrestrial Physics*, *69*(3), 362–377. https://doi.org/10.1016/j.jastp.2006.06.019

Mourenas, D., Artemyev, A. V., Zhang, X. J., Angelopoulos, V., Tsai, E., & Wilkins, C. (2021). Electron lifetimes and diffusion rates inferred from ELFIN measurements at low altitude: First results. *Journal of Geophysical Research (Space Physics)*, *126*(11), e29757. https://doi.org/10.1029/2021JA029757

Newell, P. T., Sergeev, V. A., Bikkuzina, G. R., & Wing, S. (1998). Characterizing the state of the magnetosphere: Testing the ion precipitation maxima latitude (b2i) and the ion isotropy boundary. *Journal of Geophysical Research*, *103*(A3), 4739–4746. https://doi.org/10.1029/97JA03622

Ni, B., Thorne, R. M., Horne, R. B., Meredith, N. P., Shprits, Y. Y., Chen, L., & Li, W. (2011a). Resonant scattering of plasma sheet electrons leading to diffuse auroral precipitation: 1. Evaluation for electrostatic electron cyclotron harmonic waves. *Journal of Geophysical Research*, *116*(A4), 4218. https://doi.org/10.1029/2010JA016232

Ni, B., Thorne, R. M., Meredith, N. P., Horne, R. B., & Shprits, Y. Y. (2011b). Resonant scattering of plasma sheet electrons leading to diffuse auroral precipitation: 2. Evaluation for whistler mode chorus waves. *Journal of Geophysical Research*, *116*(A4), 4219. https://doi.org/10.1029/2010JA016233

Ni, B., Thorne, R. M., Meredith, N. P., Shprits, Y. Y., & Horne, R. B. (2011c). Diffuse auroral scattering by whistler mode chorus waves: Dependence on wave normal angle distribution. *Journal of Geophysical Research*, *116*(A10), 10207. https://doi.org/10.1029/2011JA016517

Ni, B., Thorne, R. M., Zhang, X., Bortnik, J., Pu, Z., Xie, L., et al. (2016). Origins of the earth's diffuse auroral precipitation. *Space Science Reviews*, *200*(1–4), 205–259. https://doi.org/10.1007/s11214-016-0234-7

Nishimura, Y., Bortnik, J., Li, W., Thorne, R. M., Lyons, L. R., Angelopoulos, V., et al. (2010). Identifying the driver of pulsating aurora. *Science*, *330*(6000), 81–84. https://doi.org/10.1126/science.1193186

Ohtani, S., Takahashi, K., Higuchi, T., Lui, A. T. Y., Spence, H. E., & Fennell, J. F. (1998). AMPTE/CCE-SCATHA simultaneous observations of substorm-associated magnetic fluctuations. *Journal of Geophysical Research*, *103*(A3), 4671–4682. https://doi.org/10.1029/97JA03239

Qin, M., Li, W., Shen, X.-C., Angelopoulos, V., Selesnick, R., Capannolo, L., et al. (2024). Global survey of energetic electron precipitation at low earth orbit observed by ELFIN. *Geophysical Research Letters*, *51*(10), e2023GL105134. https://doi.org/10.1029/2023GL105134

Sergeev, V. A., Angelopoulos, V., Apatenkov, S., Bonnell, J., Ergun, R., Nakamura, R., et al. (2009). Kinetic structure of the sharp injection/dipolarization front in the flow-braking region. *Geophysical Research Letters*, *36*(21), 21105. https://doi.org/10.1029/2009GL040658

Sergeev, V. A., Angelopoulos, V., Kubyshkina, M., Donovan, E., Zhou, X.-Z., Runov, A., et al. (2011). Substorm growth and expansion onset as observed with ideal ground-spacecraft THEMIS coverage. *Journal of Geophysical Research*, *116*(A5), A00I26. https://doi.org/10.1029/2010JA015689

Sergeev, V. A., Bikkuzina, G. R., & Newell, P. T. (1997). Dayside isotropic precipitation of energetic protons. *Annales Geophysicae*, *15*(10), 1233–1245. https://doi.org/10.1007/s00585-997-1233-5

Sergeev, V. A., Chernyaev, I. A., Angelopoulos, V., & Ganushkina, N. Y. (2015). Magnetospheric conditions near the equatorial footpoints of proton isotropy boundaries. *Annales Geophysicae*, *33*(12), 1485–1493. https://doi.org/10.5194/angeo-33-1485-2015

Sergeev, V. A., Gordeev, E. I., Merkin, V. G., & Sitnov, M. I. (2018). Does a local B-minimum appear in the tail current sheet during a substorm growth phase? *Geophysical Research Letters*, *45*(6), 2566–2573. https://doi.org/10.1002/2018GL077183

Sergeev, V. A., & Gvozdevsky, B. B. (1995). MT-index - A possible new index to characterize the magnetic configuration of magnetotail. *Annales Geophysicae*, *13*(10), 1093–1103. https://doi.org/10.1007/s00585-995-1093-9

Sergeev, V. A., Kubyshkina, M. V., Semenov, V. S., Artemyev, A., Angelopoulos, V., & Runov, A. (2023). Unusual magnetospheric dynamics during intense substorm initiated by strong magnetospheric compression. *Journal of Geophysical Research (Space Physics)*, *128*(11), e2023JA031536. https://doi.org/10.1029/2023JA031536

Sergeev, V. A., Nishimura, Y., Kubyshkina, M., Angelopoulos, V., Nakamura, R., & Singer, H. (2012). Magnetospheric location of the equatorward prebreakup arc. *Journal of Geophysical Research (Space Physics)*, *117*(A1), A01212. https://doi.org/10.1029/2011JA017154

Sergeev, V. A., Sazhina, E. M., Tsyganenko, N. A., Lundblad, J. A., & Soraas, F. (1983). Pitch-angle scattering of energetic protons in the magnetotail current sheet as the dominant source of their isotropic precipitation into the nightside ionosphere. *Planatary Space Science*, *31*(10), 1147–1155. https://doi.org/10.1016/0032-0633(83)90103-4

Sergeev, V. A., & Tsyganenko, N. A. (1982). Energetic particle losses and trapping boundaries as deduced from calculations with a realistic magnetic field model. *Planatary Space Science*, *30*(10), 999–1006. https://doi.org/10.1016/0032-0633(82)90149-0

Sharma, A. S., Nakamura, R., Runov, A., Grigorenko, E. E., Hasegawa, H., Hoshino, M., et al. (2008). Transient and localized processes in the magnetotail: A review. *Annales Geophysicae*, *26*(4), 955–1006. https://doi.org/10.5194/angeo-26-955-2008

Shen, Y., Artemyev, A., Vasko, I., Zhang, X.-J., Angelopoulos, V., An, X., & Runov, A. (2022). Energetic electron scattering by kinetic Alfvén waves at strong magnetic field gradients of dipolarization front. *Physics of Plasmas*, *29*(8), 082901. https://doi.org/10.1063/5.0096338

Shen, Y., Artemyev, A., Zhang, X.-J., Vasko, I. Y., Runov, A., Angelopoulos, V., & Knudsen, D. (2020). Potential evidence of low-energy electron scattering and ionospheric precipitation by time domain structures. *Geophysical Research Letters*, *47*(16), e89138. https://doi.org/10.1029/2020GL089138

Shen, Y., Artemyev, A. V., Runov, A., Angelopoulos, V., Liu, J., Zhang, X.-J., et al. (2023). Energetic electron flux dropouts measured by ELFIN in the ionospheric projection of the plasma sheet. *Journal of Geophysical Research (Space Physics)*, *128*(9), e2023JA031631. https://doi.org/10.1029/2023JA031631

Shevchenko, I. G., Sergeev, V., Kubyshkina, M., Angelopoulos, V., Glassmeier, K. H., & Singer, H. J. (2010). Estimation of magnetosphere-ionosphere mapping accuracy using isotropy boundary and THEMIS observations. *Journal of Geophysical Research (Space Physics)*, *115*(A11), A11206. https://doi.org/10.1029/2010JA015354

Shi, X., Stephens, G. K., Artemyev, A. V., Sitnov, M. I., & Angelopoulos, V. (2024). Picturing global substorm dynamics in the magnetotail using low-altitude ELFIN measurements and data mining-based magnetic field reconstructions. *arXiv e-prints*, *22*(10). arXiv:2406.13143. https://doi.org/10.48550/arXiv.2406.13143

Shprits, Y. Y., Subbotin, D. A., Meredith, N. P., & Elkington, S. R. (2008). Review of modeling of losses and sources of relativistic electrons in the outer radiation belt II: Local acceleration and loss. *Journal of Atmospheric and Solar-Terrestrial Physics*, *70*(14), 1694–1713. https://doi.org/10.1016/j.jastp.2008.06.014

Shustov, P. I., Zhang, X. J., Pritchett, P. L., Artemyev, A. V., Angelopoulos, V., Yushkov, E. V., & Petrukovich, A. A. (2019). Statistical properties of sub-ion magnetic holes in the dipolarized magnetotail: Formation, structure, and dynamics. *Journal of Geophysical Research (Space Physics)*, *124*(1), 342–359. https://doi.org/10.1029/2018JA025852

Sitnov, M. I., Birn, J., Ferdousi, B., Gordeev, E., Khotyaintsev, Y., Merkin, V., et al. (2019a). Explosive magnetotail activity. Space. *Science Review*, *215*(4), 31. https://doi.org/10.1007/s11214-019-0599-5

Sitnov, M. I., Stephens, G. K., Tsyganenko, N. A., Miyashita, Y., Merkin, V. G., Motoba, T., et al. (2019b). Signatures of nonideal plasma evolution during substorms obtained by mining multimission magnetometer data. *Journal of Geophysical Research (Space Physics)*, *124*(11), 8427–8456. https://doi.org/10.1029/2019JA027037

Sorathia, K. A., Merkin, V. G., Panov, E. V., Zhang, B., Lyon, J. G., Garretson, J., et al. (2020). Ballooning-interchange instability in the near-earth plasma sheet and auroral beads: Global magnetospheric modeling at the limit of the MHD approximation. *Geophysical Research Letters*, *47*(14), e88227. https://doi.org/10.1029/2020GL088227

Sotirelis, T., & Newell, P. T. (2000). Boundary-oriented electron precipitation model. *Journal of Geophysical Research*, *105*(A8), 18655–18673. https://doi.org/10.1029/1999JA000269

Stephens, G. K., Sitnov, M. I., Korth, H., Tsyganenko, N. A., Ohtani, S., Gkioulidou, M., & Ukhorskiy, A. Y. (2019). Global empirical picture of magnetospheric substorms inferred from multimission magnetometer data. *Journal of Geophysical Research (Space Physics)*, *124*(2), 1085–1110. https://doi.org/10.1029/2018JA025843

Summers, D. (2005). Quasi-linear diffusion coefficients for field-aligned electromagnetic waves with applications to the magnetosphere. *Journal of Geophysical Research*, *110*(A8), 8213. https://doi.org/10.1029/2005JA011159

Tao, X., Thorne, R. M., Li, W., Ni, B., Meredith, N. P., & Horne, R. B. (2011). Evolution of electron pitch angle distributions following injection from the plasma sheet. *Journal of Geophysical Research*, *116*(A4), A04229. https://doi.org/10.1029/2010JA016245

Thorne, R. M., Bortnik, J., Li, W., & Ma, Q. (2021). Wave–particle interactions in the earth's magnetosphere. In *Magnetospheres in the solar system* (pp. 93–108). American Geophysical Union (AGU). https://doi.org/10.1002/9781119815624.ch6

Tsai, E., Artemyev, A., Ma, Q., Mourenas, D., Agapitov, O., Zhang, X.-J., & Angelopoulos, V. (2024a). Key factors determining nightside energetic electron losses driven by whistler-mode waves. *Journal of Geophysical Research (Space Physics)*, *129*(3), e2023JA032351. https://doi.org/10.1029/2023JA032351

Tsai, E., Artemyev, A., Zhang, X.-J., & Angelopoulos, V. (2022). Relativistic electron precipitation driven by nonlinear resonance with whistler-mode waves. *Journal of Geophysical Research (Space Physics)*, *127*(5), e30338. https://doi.org/10.1029/2022JA030338

Tsai, E., Palla, A., Norris, A., King, J., Russell, C., Ye, S., et al. (2024b). *Remote sensing of electron precipitation mechanisms enabled by ELFIN mission operations and ADCS design*. Engineering Archive. https://doi.org/10.31224/3487

Tsyganenko, N. A. (1989). A magnetospheric magnetic field model with a warped tail current sheet. *Planatary Space Science*, *37*(1), 5–20. https://doi.org/10.1016/0032-0633(89)90066-4

Tsyganenko, N. A., & Andreeva, V. A. (2015). A forecasting model of the magnetosphere driven by an optimal solar wind coupling function. *Journal of Geophysical Research (Space Physics)*, *120*(10), 8401–8425. https://doi.org/10.1002/2015JA021641

Ukhorskiy, S., & Millan, R. (2024). Unveiling the mysteries of multiscale magnetotail dynamics with the CINEMA constellation. In *Egu general assembly conference abstracts*. https://doi.org/10.5194/egusphere-egu24-13286.13286

West, H. I., Buck, R. M., & Kivelson, M. G. (1978). On the configuration of the magnetotail near midnight during quiet and weakly disturbed periods: Magnetic field modeling. *Journal of Geophysical Research*, *83*(A8), 3819–3831. https://doi.org/10.1029/JA083iA08p03819

Wilkins, C., Angelopoulos, V., Runov, A., Artemyev, A., Zhang, X. J., Liu, J., & Tsai, E. (2023). Statistical characteristics of the electron isotropy boundary. *Journal of Geophysical Research (Space Physics)*, *128*(10), e2023JA031774. https://doi.org/10.1029/2023JA031774

Wing, S., & Newell, P. T. (1998). Central plasma sheet ion properties as inferred from ionospheric observations. *Journal of Geophysical Research*, *103*(A4), 6785–6800. https://doi.org/10.1029/97JA02994

Yahnin, A. G., Yahnina, T. A., Raita, T., & Manninen, J. (2017). Ground pulsation magnetometer observations conjugated with relativistic electron precipitation. *Journal of Geophysical Research (Space Physics)*, *122*(9), 9169–9182. https://doi.org/10.1002/2017JA024249

Yando, K., Millan, R. M., Green, J. C., & Evans, D. S. (2011). A Monte Carlo simulation of the NOAA POES medium energy proton and electron detector instrument. *Journal of Geophysical Research (Space Physics)*, *116*(A10), A10231. https://doi.org/10.1029/2011JA016671

Yang, J., Wolf, R. A., Toffoletto, F. R., Sazykin, S., & Wang, C.-P. (2014). RCM-E simulation of bimodal transport in the plasma sheet. *Geophysical Research Letters*, *41*(6), 1817–1822. https://doi.org/10.1002/2014GL059400

Yue, C., Bortnik, J., Thorne, R. M., Ma, Q., An, X., Chappell, C. R., et al. (2017). The characteristic pitch angle distributions of 1 ev to 600 kev protons near the equator based on van allen probes observations. *Journal of Geophysical Research*, *122*(9), 9464–9473. Retrieved from https://doi.org/10.1002/2017JA024421

Yue, C., Wang, C.-P., Lyons, L., Liang, J., Donovan, E. F., Zaharia, S. G., & Henderson, M. (2014). Current sheet scattering and ion isotropic boundary under 3-D empirical force-balanced magnetic field. *Journal of Geophysical Research*, *119*(10), 8202–8211. https://doi.org/10.1002/2014JA020172

Zhang, X.-J., Angelopoulos, V., Mourenas, D., Artemyev, A., Tsai, E., & Wilkins, C. (2022). Characteristics of electron microburst precipitation based on high-resolution ELFIN measurements. *Journal of Geophysical Research (Space Physics)*, *127*(5), e30509. https://doi.org/10.1029/2022JA030509

Zhang, X.-J., Angelopoulos, V., Ni, B., & Thorne, R. M. (2015). Predominance of ECH wave contribution to diffuse aurora in Earth's outer magnetosphere. *Journal of Geophysical Research*, *120*(1), 295–309. https://doi.org/10.1002/2014JA020455

Zhang, X.-J., Artemyev, A., Angelopoulos, V., & Horne, R. B. (2017). Kinetics of sub-ion scale magnetic holes in the near-earth plasma sheet. *Journal of Geophysical Research*, *122*(10). Retrieved from https://doi.org/10.1002/2017JA024197

Zou, Y., Zhang, X.-J., Artemyev, A. V., Shen, Y., & Angelopoulos, V. (2024). The key role of magnetic curvature scattering in energetic electron precipitation during substorms. *Geophysical Research Letters*, *51*(14), e2024GL109227. https://doi.org/10.1029/2024GL109227